Master's thesis

Geography

Geoinformatics

Classification of agricultural crops of the Taita Hills, Kenya using airborne AisaEAGLE imaging spectroscopy data

Rami Piiroinen

2014

Supervisors:
Petri Pellikka
Matti Mõttus

UNIVERSITY OF HELSINKI
DEPARTMENT OF GEOSCIENCES AND GEOGRAPHY
DIVISION OF GEOGRAPHY

PO box 64 (Gustaf Hällströmin katu 2)
FIN-00014 Helsingin yliopisto

TABLE OF CONTENTS

LIST OF FIGURES

LIST OF TABLES

ABBREVIATIONS

AGL	Above Ground Level
AISA	Airborne Imaging Spectrometer for Applications
ARVI	Atmospherically resistant vegetation index
ASCII	American Standard Code for Information Interchange
ASD	Analytical Spectral Devices inc.
ATCOR-4	Atmospheric Correction 4 program
AVIRIS	Airborne Visible Infrared Imaging Spectrometer
BIL	ENVI Band Interleaved by Line data format
BRDF	Bidirectional reflectance distribution function
CCD	Charge-coupled device
BSQ	ENVI Band Sequental data format
CHIESA	The Climate Change Impacts on Ecosystem Services and Food Security in Eastern Africa
DEM	Digital Elevation Model
DN	Digital Number
EABH	Eastern Afromontane Biodiversity Hotspot
EGM96	Earth Gravitational Model 1996
EVI	Enhanced Vegetation Index
EC	Error of commission
EO	Error of omission
FLAASH	Fast Line-of-sight Atmospheric Analysis of Spectral Hypercubes
FOV	Field of view
FODIS	Fibre Optic Downwelling Irradiance Sensor
FWHM	Full width half maximum
GB	Gigabyte
GPS	Global Positioning System
ICIPE	International Centre of Insect Physiology and Ecology
IMU	Inertial Motion Unit
LiDAR	Light Detection and Ranging
MNF	Minimum Noise Fraction
MODTRAN	Moderate Resolution Atmospheric Radiance and Transmittance Model
NIR	Near infrared spectral region

NVI	Normalized Vegetation Index
OA	Overall accuracy
PA	Producer’s accuracy
PCA	Primary Component Analysis
RENDVI	Red Edge Normalized Difference Vegetation Index
STD	Standard deviation
SVM	Support Vector Machine
SWIR	Short wave infrared spectral region
UA	User’s accuracy
UTC	Coordinated Universal Time
UTM	Universal Transverse Mercator (projection)
VNIR	Visible and near infrared spectral region
WGS84	World Geodetic System 1984

1. INTRODUCTION

1.1 Crop classification for studying land use practices and food production

Studies have shown that anthropogenic changes in land cover/land use are having local, regional and even global consequences (Foley et al. 2005). The change in the land use practices is happening at a fast pace especially in the tropics. In Africa 16% of forests and 5% of its woodlands and grasslands were lost during the period of 1975–2000. At the same time agricultural land increased by 57% in sub-Saharan Africa (Pellikka et al. 2013; Brink and Eva 2009). Forests, woodlands and bushlands are being transformed for agricultural use to produce food for the rapidly growing population. In the population grew from 6 million in 1950 to 41 million in 2010 (United Nations 2014). Although food production is crucial for the survivability of the people the uncontrolled expansion of agricultural land at the expense of natural habitats may first increase food production but in the longer term actually decrease it (Foley et al. 2005). This is due to disturbances in water balance, increased land erosion and eradication of natural habitats for pollinators.

In the Taita Hills, Kenya previous studies on the land use/land cover change have been done by Pellikka et al. (2009) and Clark & Pellikka (2009) among others. These studies have shown that during the past decades, cropland areas have mainly expanded at the expense of shrublands and thickets especially in the lower foothill areas of the Taita Hills. Some forest areas are also converted for agricultural use in the higher altitudes, but this has amounted only 20 ha of the total increase of 10 478 ha of cropland areas during the period of 1987 to 2003. These studies show the transformation of forests, woodlands or bushlands to agricultural use, but they do not have information of the actual food crops that are being farmed. This information is needed to further understand the local land use practices and their impacts on the ecosystem and food production. In best case scenarios it is possible to achieve environmental, social and economic benefits by optimizing the land use practices (Foley et al. 2005). This is only possible if the full ecosystem functionality is well understood. The first step to achieve this understanding is to map land cover as accurately as possible.

Land use/land cover in the Taita Hills have been mapped using remote sensing technologies as there are no other source of accurate information of land use available. Pellikka et al. (2009) used airborne black and white, and RGB cameras for their study and Clark & Pellikka (2009) used multispectral satellite imagery. These are traditional remote

sensing methods that are not capable of accurate crop classifications (Nagendra & Rocchini 2008). Although multispectral SPOT satellite imagery used by Clark & Pellikka (2009) could be used for species specific classification to a certain degree (Verbeiren 2008). One possibility would be to use satellite based Hyperion data that has been used for crop classifications (Galvão et al. 2012). However these methods are not well suited for the Taita Hills, where fields are small and multi-cropping system is used, as the spatial resolution of Hyperion data is too low. The optimum method for crop classification in the case of the Taita Hills, Kenya is airborne imaging spectroscopy that showed superior classification accuracy compared to Hyperion data in a study by Ghosh et al. (2014).

1.2 CHIESA project

This thesis was made within Climate Change Impacts on Ecosystem Services and Food Security in Eastern Africa (CHIESA 2014) project. CHIESA is a research and development project aimed at increasing the knowledge of the impacts of climate change on ecosystem services in the Eastern Afromontane Biodiversity Hotspot (EABH) ranging from Ethiopia to Tanzania through the Taita Hills, Kenya. CHIESA is funded by the Ministry of Foreign Affairs of Finland (FORMIN 2014), and coordinated by International Centre of Insect Physiology and Ecology (ICIPE 2014) in Nairobi, Kenya. The project is divided into eight work packages in the primary fields of agriculture, hydrology, ecology and geoinformatics. This thesis is part of work package 2 – Land Use and Biogeophysical Information. In this work package satellite imagery and airborne remote sensing data is applied to land cover mapping and change detection.

1.3 Objectives

The main objective of this thesis is to develop a method for crop classification using high spatial and spectral resolution AisaEAGLE (Specim 2012) imaging spectroscopy data acquired in January of 2012 in the Taita Hills, Kenya. The developed method will then be shared with other participants in the CHIESA project.

Second objective is to develop the process of planning and executing imaging spectroscopy data acquisition campaigns in rural African landscape. The acquired knowledge and the resulting land cover information within the Taita Hills is then shared with the CHIESA project and the University of Helsinki research team.

1.4 Workflow

This thesis will go through all the steps from planning the flight campaign, processing the data and analyzing the results. The main steps are described in Figure 1. First a flight plan was that covered the CHIESA study transect was made and study plots were planned along this transect. Based on these plans a field campaign was conducted in the study area in January–February of 2012. The flight campaign resulted in AisaEAGLE raw data and Nikon D3X images. Nikon D3X images were printed after the flights and were used for the field mapping of the study plots. These maps were then digitized and used as reference material when training and testing samples were collected from AisaEAGLE imagery for the classification procedure. AisaEAGLE raw data was radiometrically, geometrically and atmospherically corrected to georeferenced image mosaic in reflectance values. Minimum noise fraction (MNF) transformation was applied to the data to reduce the noise and dimensionality. MNF transformed data was classified based on the training samples collected from the study plots. Accuracies of the classifications were assessed with testing samples that were collected from the same plots. The results of this thesis are drawn from this procedure and the results of the classification.

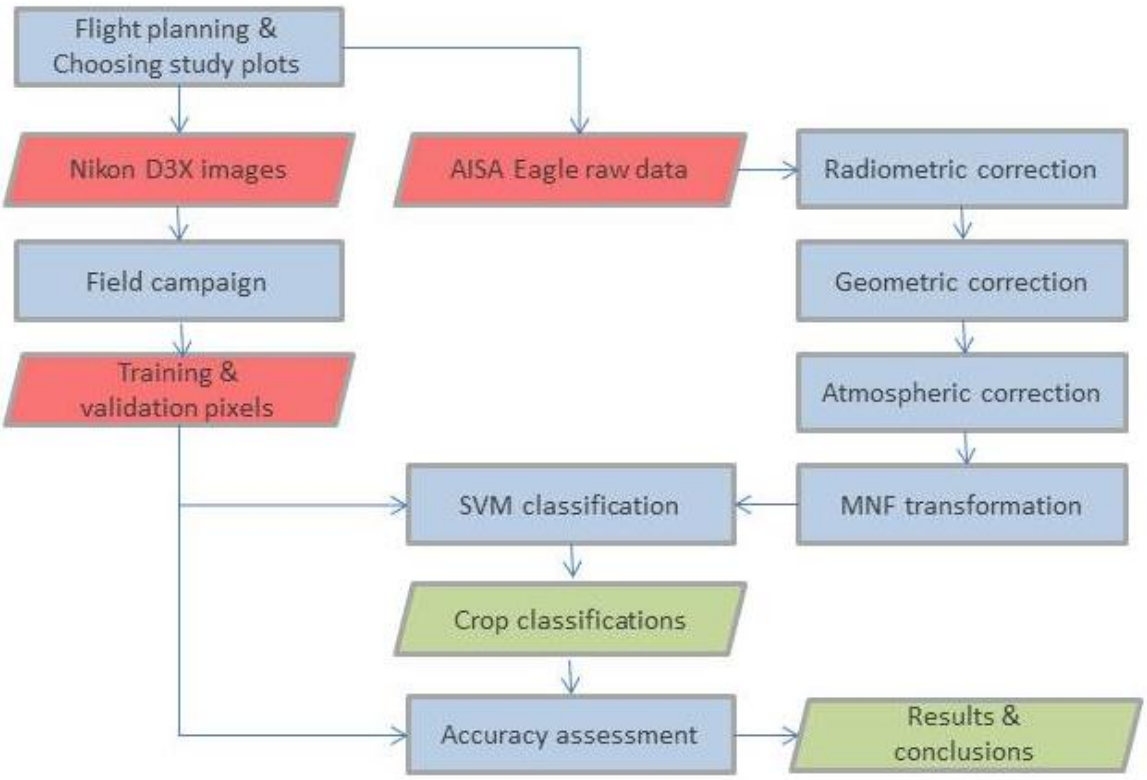

Figure 1. Workflow of the thesis.

2. BACKGROUND

2.1 Imaging spectroscopy

The foundation for imaging spectroscopy was laid when Sir Isaac Newton published the concept of dispersion of light in "Treatise of Light" (Schaepman 2009). He was the first to explain scientifically how light is dispersed by a prism. Newton's theory was later succeeded by wave theory resulting in James Maxwell's equations of electromagnetic waves. These theories are the historical basis of spectroscopy that is defined by Schaepman (2009: 167) as: "*The study of light as a function of wavelength that has been emitted, reflected, or scattered from a solid, liquid, or gas.*" Imaging spectroscopy is an extension of spectroscopy where the dispersed light is recorded as images. Schaepman et al. (2006) defined it as: *"The simultaneous acquisition of spatially coregistered images, in many, spectrally contiguous bands, measured in calibrated radiance units, from a remotely operated platform".* AisaEAGLE sensor used in this study is an imaging spectrometer designed for airborne imaging spectroscopy (Specim 2012). In remote sensing the term hyperspectral is used interchangeably with spectroscopy. It denotes the presence of large amount of spectral bands without further specification (Schaepman 2009).

2.2 Physical background of remote sensing

2.2.1 Electromagnetic radiation

James Maxwell (1831–1879) conceptualized electromagnetic radiation as an electromagnetic wave that travels through vacuum of space at the speed of light (c = 3 * 10^8 meters per second) (Jensen 2000: 30). In Maxwell's theory wavelength (λ) is depended upon the time that the charged particle is accelerated. It is defined as the mean distance between maximums of the waves parallel to the direction where the light is travelling. Wavelength is commonly expressed as nanometers (nm) or microns (µm) in visible and near-infrared (VNIR) spectral region while 1 µm equals to 1000 nm. Frequency (v) is the number of wavelengths passing a point per unit time and it depends on the number of accelerations per second (Jensen 2000: 30). Frequency is inversely proportional to wavelength:

$$c = \lambda v$$

Maxwell's wave theory can describe the behavior of electromagnetic radiation in vacuum, but when it interacts with matter, the situation changes. Albert Einstein concluded that when electromagnetic radiation interacts with electrons/matter it behaves like it is composed of individual bodies called photons that carry particle like properties as energy and momentum (Jensen 2000: 35).

Quantum theory by Niels Bohr and Max Planck states that energy is transferred in discrete packets called quanta or photons (Jensen 2000: 37). The energy of a quantum is inversely proportional to its wavelength, which links the particle theory to wave theory. When matter is heated to so high temperatures that electrons break off from their orbits the remaining nucleus is called ion. When free electron falls back to fill the vacant orbit then the radiation given off is in continuous spectrum rather than in specific wavelength or band. Hot surface of Sun produces this continuous spectrum of radiation, which travels to Earth on a spectral range from gamma rays to very long radio waves. The relationship between frequency in wave theory and quantum energy is:

$$Q = hv$$

Where Q is the energy of quantum measured in Joules (J), h is Planck constant ($6.626 * 10^{-34}$ J s), v is the frequency of the radiation.

Most of the electromagnetic radiation recorded by remote sensing systems originates from the Sun, but all objects above 0 Kelvin (K) emit electromagnetic energy. Electromagnetic radiation emitted by an opaque and non/reflective body held at constant uniform temperature is called blackbody radiation. Electromagnetic spectrum of the Sun is close to blackbody radiation of 6000 K object. Intensity peak of radiation originating from the Sun is in the visible light region around 480 nm (Figure 2) whereas Earth has intensity peak at around 9.66 µm, which is commonly referred to as the thermal region.

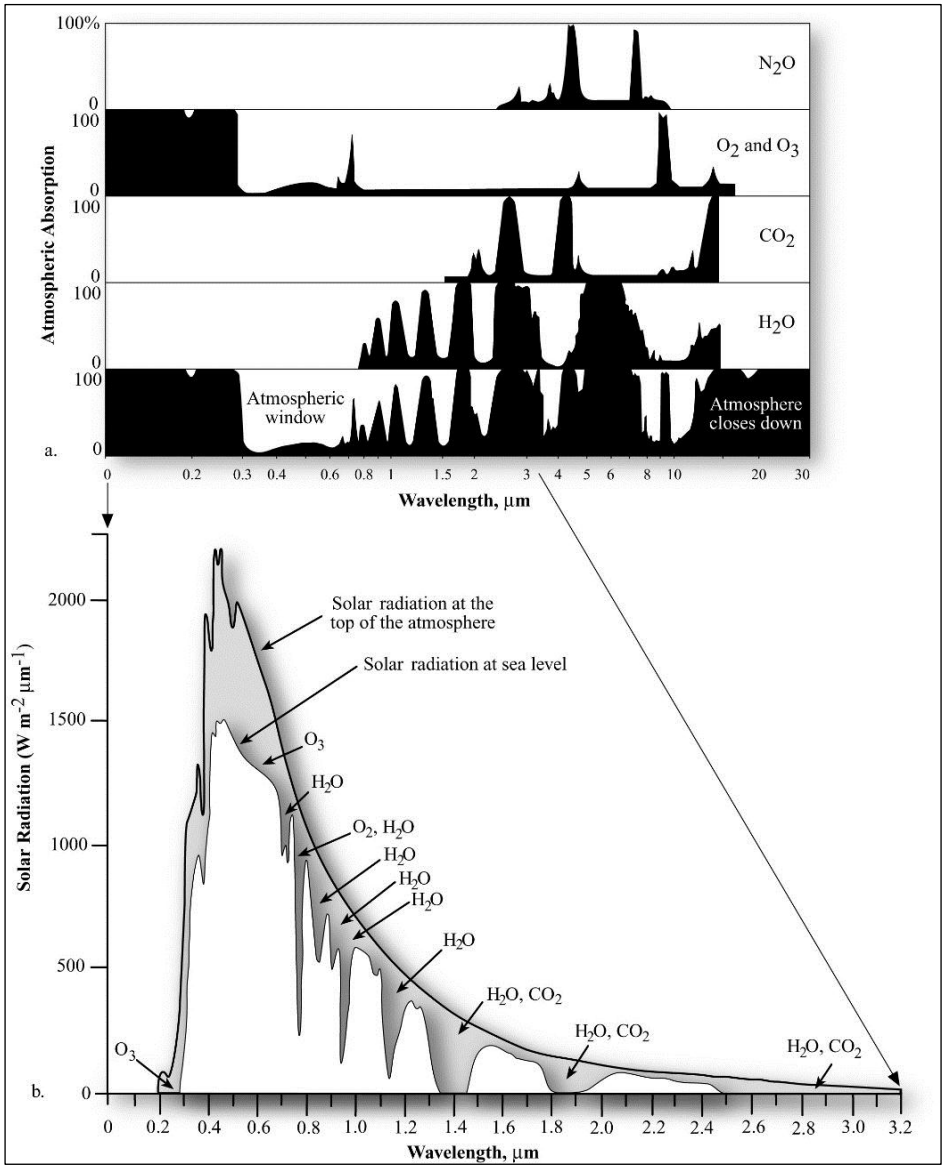

Figure 2. Solar radiation spectrum at the top of the atmosphere and at sea level (bottom) and the main agents causing atmospheric absorption (top). Original figure from the book The Remote Sensing of the Environment by John Jensen (2000: 40).

2.2.2 Energy-matter interactions in the atmosphere

Refraction is caused when the speed of light alters in substances with different density (Jensen: 40). This happens when the radiant energy from the Sun reaches the Earth's atmosphere after travelling in the vacuum of space. Index of refraction *n* is:

$$n = \frac{c}{c_n}$$

Where c is the speed of light and c_n is the speed of light in substance.

Scattering occurs when gases and small particles in the atmosphere absorb and reemit radiation. Rayleigh scattering occurs when the diameter of the particles are smaller than the wavelength of the incident radiation. In optical remote sensing this causes problems when blue wavelengths interact with oxygen and nitrogen in the upper 4.5 km of atmosphere (Jensen 2000: 41; Aggarwal 2004: 35). Mie scattering occurs in the lower 4.5 km of the atmosphere when wavelength of the incoming radiation is similar to the size of the atmospheric particles. In visible light spectral region the main agents causing Mie scattering are dust, smoke and microscopic water droplets. Non-selective scattering occurs in the lowest portion of the atmosphere when particles are 10 times the wavelength of the incident radiation. Because of the large size of the particles non-selective scattering affects all the wavelengths of incident radiation in visible and near-infrared (VNIR) spectral region (Jensen 2000: 42; Aggarwal 2004: 36). Absorption is the process where radiant energy is absorbed and converted into other forms of energy. In VNIR spectral region the main substances causing atmospheric absorption are water vapor, oxygen, ozone and nitrous oxide (Figure 2).

2.2.3 Radiance paths

Ideally in remote sensing only the radiant energy originating from the target would be measured in the IFOV of the sensor (Jensen 2000: 48). This is rarely the case as scattering, absorption and reemission of the radiant energy in the atmosphere causes radiant energy from other sources to hit the sensor from the same solid angle. These various radiance paths are described in Figure 3 and explained based on the work by Jensen (2000: 49–51).

Path 1 contains solar irradiance (E_o) that has attenuated only little before illuminating the terrain within IFOV. If all of the E_o from a specific solar zenith angle (θ_o) reaches the surface then atmospheric transmittance at this angle ($T_{\theta o}$) equals to one.

Path 2 contains the diffuse sky irradiance (E_d) that never reaches the surface before scattering in the atmosphere and changing path to the sensor IFOV. This is mainly caused by Rayleigh scattering and affects especially the blue wavelengths.

Path 3 contains radiant energy from the Sun that has undergone scattering, absorption or reemission before illuminating the study area. It has different spectral composition and polarization than the radiant energy from Path 1.

Path 4 contains radiant energy that has reflected from neighboring area and changed its direction in the atmosphere to the IFOV of the sensor.

Path 5 contains radiant energy that is reflected from neighboring area and scattered back to the study area from the atmosphere.

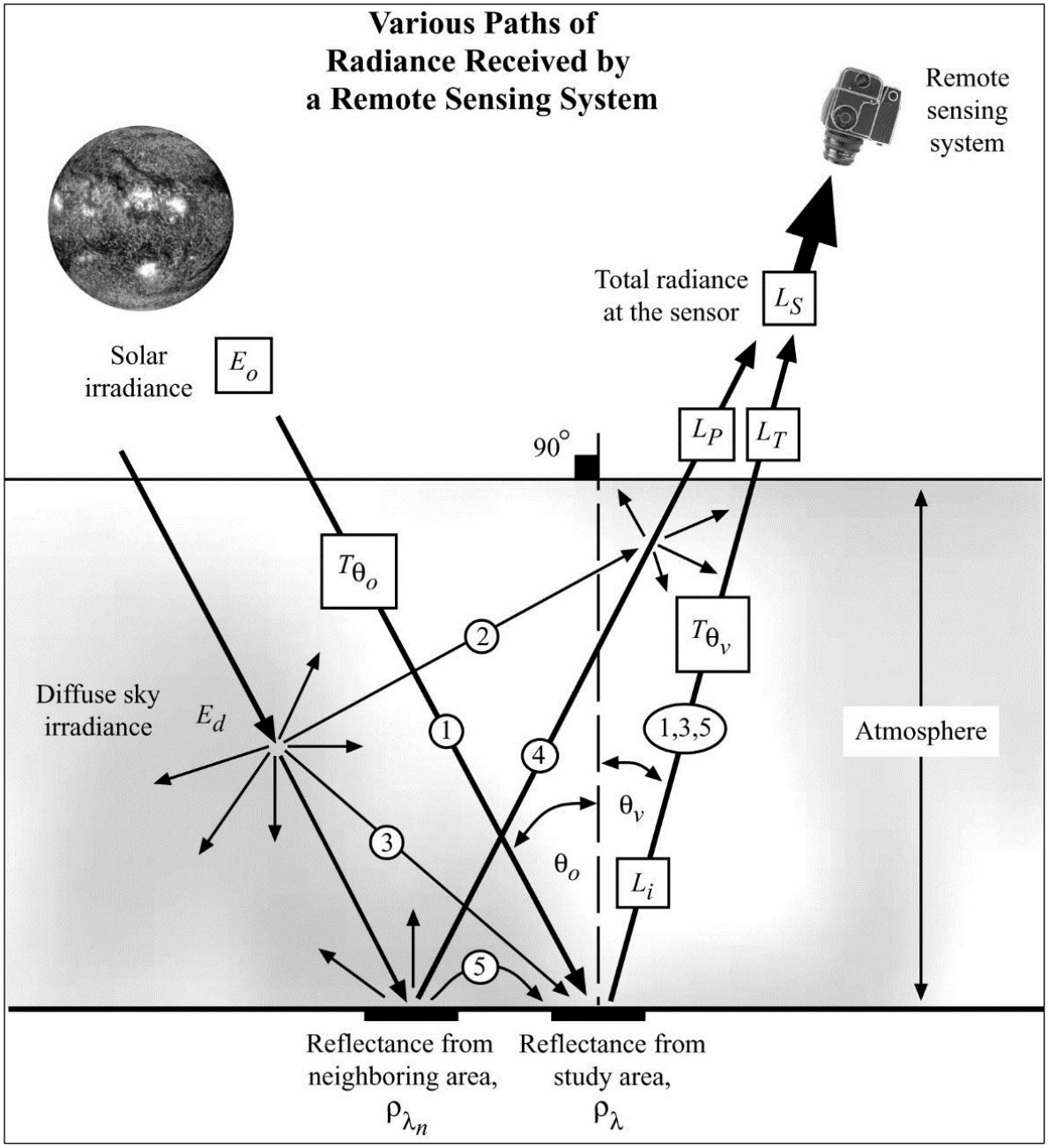

Figure 3. Various radiance paths received by remote sensing systems. Original figure is from the book The Remote Sensing of the Environment by John Jensen (2000: 51).

2.2.4 Terminology related to the measurement of the solar energy

Radiant flux (Φ_e) is the radiant energy onto, off of, or through a surface per unit time measured in units of W (Jensen: 44).

Radiance (L_e) is the radiant flux per unit solid angle leaving an extended source in a given direction per unit of projected source area in that direction measured in units of W m^{-2} sr^{-1} (Jensen 2000: 47; Pravlov 2011):

$$L_e = \frac{\mathrm{d}^2 \Phi_e}{\mathrm{d}A \mathrm{d}\Omega \cos\theta}$$

Where:

d is the differential operator
Φ_e is the radiant flux (W)
θ is the angle between the surface normal and the specified direction
A is the area of the surface (m^2)
Ω is the solid angle (steradian) subtended by the observation or measurement

Spectral radiance $L_e(\lambda)$ is the radiance per wavelength unit measured in units of W m^{-2} sr^{-1} nm (Pravilov 2011):

$$L_e(\lambda) = \frac{\mathrm{d}L_e}{\mathrm{d}\lambda}$$

Where λ is light (radiation) wavelength

Irradiance E_e is the ratio of the radiant power falling on the radiant surface element to the value of the element measured in units of W m^{-2} (Pravilov 2011):

$$E_e = \frac{\mathrm{d}\Phi_e}{\mathrm{d}S}$$

Where S is the area of the surface element

Spectral irradiance $E_e(\lambda)$ is the irradiance per wavelength unit measured in units of W m^{-2} nm (Pravilov 2011):

$$E_e(\lambda) = \frac{\mathrm{d}E_e}{\mathrm{d}\lambda}$$

Reflectance ρ is the dimensionless ratio of the radiant flux reflected from a surface to the radiant flux incident to it (Schaepman-Strub et al. 2006):

$$\rho = \frac{\Phi_r}{\Phi_i}$$

Where:

Φ_r is the radiant flux reflected from a surface
Φ_i is the radiant flux incident to a surface

2.3 Biophysical foundation of the spectral properties of vegetation

Life on Earth is depended on photosynthesis that produces organic matter and oxygen. Kiang et al. (2007) demonstrated in their study how the characteristic reflectance patterns vary among different taxonomic groups of photosynthetic organisms in VNIR (visible and near infrared) spectral region. For example plants, lichens and algae groups have very distinct reflectance curves. The spectral differences between species in the terrestrial plants group are not as dramatic but still significant.

The main absorption features in VNIR spectral region for green vegetation are caused by plant pigments such as chlorophyll a and b, carotenoids and anthocyanins, and plant water (Ustin et al. 2009; Jensen 2000). Chlorophyll pigments are located inside chloroplast, in palisade cells of mesophyll. Here the chlorophyll a and b pigments are capturing incident solar radiation and using this energy to transform water and carbon dioxide to carbohydrates and oxygen. Chlorophyll a has absorption maximums around 430 and 662 nm and chlorophyll b around 453 and 642 nm, when the measurements are made for isolated pigments extracted in diethyl ether. These absorption valleys are causing the green color of healthy green vegetation with high photosynthetic activity (Clevers et al. 2002). Carotenoids have absorption maximums around 451 and 470 nm when extracted in hexane. Carotenoids have variety of functions in plants. For example xanthophylls are protecting plants from photo-oxidation and photoinhibition caused by excess radiation. Anthocyanins have single absorption maximum around 529 nm (Ustin et al. 2009). Anthocyanins also protect the plants from excess radiation and may provide protection from herbivore and fungal pathogens. After the second chlorophyll absorption maximum the reflectance increases dramatically towards NIR region (Gates et al. 1965). This steep rise is called the red edge (Baranoski & Rokne 2005). If the leaves would absorb radiation in NIR region

with same intensity as in visible light region it would cause plants to overheat and plant proteins would denature causing the plant to die (Gates et al. 1965). Plant water has absorption feature at 970 nm (Peñuelas et al. 1993). Asner & Martin (2009) have showed that tropical tree species have unique compositions of these pigments, plant water and nitrogen and phosphorus that can be used for identification of species using imaging spectroscopy.

Plant pigment and water vapor compositions are depended on the season and the climatic conditions. When plants are under environmental stress or the senescence is starting the chlorophyll activity slows down and carotenoids become more visible and turn the color of the leaves to yellow and orange (Ustin et al. 2009). This causes red edge inflection point to move towards shorter wavelengths. Carotenoids are present also in healthy vegetation whereas ome plants start to produce anthocyanin heavily only in the fall, causing the bright red colors. Finally leaves will turn brown and the effect of plant pigments on the reflectance diminishes. The effect of brown plant material in stems and dry leaves increases and the main absorbing elements are cellulose and lignin (Elvidge 1990). Cellulose is the most abundant organic compound in terrestrial ecosystems and it forms around one third to half of all dry plant material. It has absorption peaks around 1.22, 1.48, 2.28, 2.34 and 2.48 µm in NIR / SWIR (shortwave infrared) region. Lignin forms around 10–35% of all dry plant matter. It has strong absorption in ultraviolet region of 0.28 µm that extends as a wing across the visible region to NIR region. The main absorption regions for cellulose and lignin are found in the thermal infrared region.

The three dimensional structure of the plants have significant effect on their spectral characteristics. In NIR region normal green leaf may have 10% absorption, 40–60% reflectance and 40–60% transmittance. This causes leaf additive reflectance when the first layer of leaves transmits light to the lower set of leaves. From these lower leaves light reflects back through first layer of leaves. This causes the NIR region reflectance to be higher in multilayered green vegetation than on a single leaf scale (Jensen 2000). Peltoniemi et al. (2005) showed how typical boreal and subartic land cover types have highly anisotropic reflectance signatures. The measurements were made with field goniometer for shrubs like blueberry and lingonberry. This means that the measured reflectance depends on the direction of where the target is viewed and the direction where the solar irradiance is coming. Rautiainen et al. (2008) have reported similar anisotropic behavior in hemiboreal tree canopies measured with multiangular CHRIS (Compact High Resolution Imaging Spectrometer) PROBA (Project for On-Board Autonomy) data. The

study also showed how the effect of background vegetation to the target signal was dependent on the viewing angle.

2.4 Managing high dimensionality of imaging spectroscopy data

Hyperspectral datasets produced with imaging spectrometers contain detailed spectral information of each pixel. This is an advantage when specific biochemical measurements are needed (Ustin 2013) or when the data is used for classification in species specific level (Ghosh et al. 2014; Asner & Martin 2009). However in some cases when the number of bands increases the classification accuracy can actually decrease (Alonso et al. 2011). This phenomenon is called the curse of dimensionality as first used by Bellman (1961) or Hughes phenomenon based on statistical analysis by Hughes (1968). The reason for this is that as the number of dimensions increase the training data becomes sparser in the multidimensional feature space.

Melgani et al. (2004) showed four possible solutions to overcome this problem: regularization of the sample covariance matrix, adaptive statistics estimation by the exploitation of the classified samples, preprocessing techniques based on feature selection or extraction, aimed at reducing or transforming the original feature space into another space of lower dimensionality or analysis of the spectral signatures to model the classes. In this thesis the problem is approached by transforming the original feature space into another space of lower dimensionality with minimum noise fraction (MNF) transformation.

MNF transformation was introduced by Andrew Green (Green et al. 1988) as an extension of the traditional principal components analysis (PCA) transformation, which does not always give the best result with large number of bands. The problem with PCA is that it maximizes the variance in the data, but not necessarily signal-to-noise ratio (SNR). MNF was designed so that after the transformation the first new band will have the highest possible SNR and the following bands will have lower SNR with increasing noise (Canty 2010). This way the important information is found on the first bands and the rest can be left out from the classification. This reduces the dimensionality of the feature space, which is expected to increase the classification accuracy.

2.5 Classification of plant species from hyperspectral data

In remote sensing the mapping of plant species has traditionally been based on aerial photo interpretation and moderate-resolution satellite image classification (Pu 2008). Aerial photo interpretation is dependent on the experience of the interpreter, which may cause large differences between the mapping results of individual interpreters. Manual interpretation is also time consuming and not cost effective (Pu 2008).

Airborne imaging spectroscopy offers abundance of spectral information in narrow contiguous bands, which allows the identification of plant species directly from the spectral properties. This will work in the cases where the spectral variance between species is greater than within species (Asner et al. 2009). The classification can be done on bands that are in radiance or reflectance values or these bands can be further processed with noise reduction and band decorrelation algorithms such as PCA or MNF transformations.

Xiao et al. (2004) reached 70% overall accuracy for their classification of 16 tree species with hyperspectral AVIRIS data gathered from city of Modesto, California in the year of 1998. They used at-sensor radiance values in their classification with the assumption that all the spectral differences are due to surface properties. Spectral library was created for the tree species based on in-situ mapping. Only 131 of 224 bands were used and the remaining bands were identified to have low spectral information content for vegetation classification. Before classification spectral mixture analysis (SMA) was used to identify the endmember fractions for each tree species from heterogeneous signals. SMA is based on assumption that each pixel is linear summation of different spectral components such as the tree crown and the underlying ground vegetation. Best results were achieved when the tree crowns were large and symmetrical with spectrally pure pixels.

Galvão et al. (2012) made a study of discriminating coffee, sugarcane, rice, common bean, corn and soybean from Hyperion dataset. Hyperion data consisted of 196 bands with 10 nm intervals in 426–2395 nm range that were atmospherically corrected to surface reflectance values with FLAASH (Fast Line-of-sight Atmospheric Analysis of Spectral Hypercubes) algorithm before classification. The study compared the overall accuracy of the classification when it was done on different wavelength regions or narrowband vegetation indices (NVI). Used method was multiple discriminant analysis (MDA). Study showed that best results were achieved in NIR–1 (791–900 nm) and SWIR–1 (1401–1900 nm) regions. Other important regions were red and green. NIR–1 region alone gave close to 80% overall accuracy. For NVIs MDA gave over 55% accuracy when the classification

was based on atmospherically resistant vegetation index (ARVI), enhanced vegetation index (EVI) and red edge normalized difference vegetation index (RENDVI). ARVI and EVI are indicators for greenness and leaf pigments and were calculated from NIR–1 and green regions. RENDVI is indicator of chlorophyll calculated from red edge region (701–760 nm).

Ghosh et al. (2014) reached 95% classification accuracy of five tree species using two airborne HyMAP imaging spectrometers with 4 meter spatial resolution covering both VNIR and SWIR spectral ranges. Study showed that MNF transformation before support vector machine (SVM) classification significantly improved the classification results. Overall accuracy with reflectance values reached just above 80% while the results on same dataset after MNF transformation reached up to 95% overall accuracy. The results from these studies indicate that SVM classifier used with MNF transformation has strong potential in the classification of plant species from imaging spectroscopy data.

3. STUDY AREA

The Taita Hills are the northern most part of the Eastern Arc Mountain range in East Africa. The hills cover an area of around 1000 square kilometers in the district of Taita Taveta in the Coast Province of Kenya (Figure 4; Pellikka et al. 2013). The massif of the Taita Hills rises from the dry savannah plane from the altitude of around 600–900 meters above sea level to the altitude of 2208 meters at the highest peak of Vuria (Pellikka 2005). These fertile mountains are surrounded by the dry bushlands of Tsavo East and Tsavo West National parks (Soini 2005; Pellikka 2005). Most significant town and the administrative center of the area is Wundanyi, which is also the location for University of Helsinki's Taita research station (Taita Research Station 2014). In prehistorical times the Taita Hills may have been covered with hundreds of square kilometers of indigenous rainforest that have since been cleared for agriculture (Pellikka et al. 2013). Now there are only few indigenous forest patches left in the highest peaks and most of the area is converted to the use of agriculture, agroforestry and human habitation (Pellikka et al. 2009). The population of the Taita Taveta district has grown from 90 000 persons in 1962 to over 300 000, which has been the driving factor behind the land use change (Pellikka et al. 2013).

Figure 4. Location of the Taita Hills in the Coast Province of Kenya.

Study area of this thesis was narrowed down to the southern part of the CHIESA main study transect (CHIESA 2014) near the town of Mwatate (860 m) (Figure 5; Soini 2006). This area was chosen since it is relatively flat and has moist valley bottom where plenty of agricultural crops were found. Study area is located in the Livestock-Millet agroecological zone that is defined to cover the elevations between 790–980 meters (Soini 2005; Jaetzold & Schmidt 1983). The annual rainfall in this zone is 480–700 mm received primarily during two rainy seasons. The longer rains occur in March–May and the shorter in September–October (Jaetzold & Schmidt 1983).

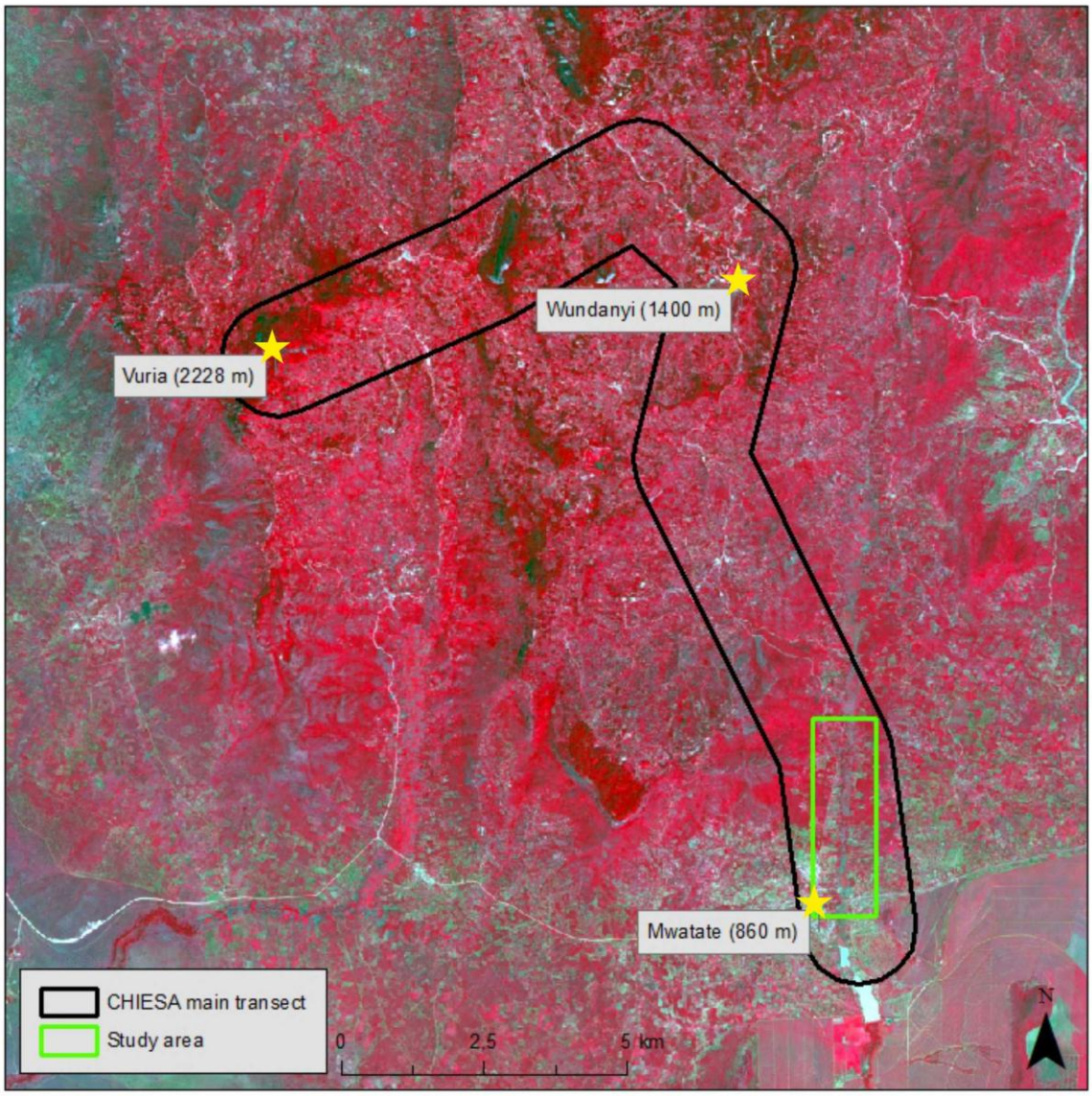

Figure 5. The location of the study area in the southern end of the main study transect of CHIESA project in the Taita Hills. The base map is false color SPOT image from 15th of October 2003.

4. MATERIAL

4.1 AisaEAGLE imaging spectrometer

AisaEAGLE is a pushbroom type imaging spectrometer that is used in research, commercial use and public services. Applications include forestry management, vegetation studies, environmental investigations, precision farming, target identification and water assessment (Specim 2012). The specific sensor used in this campaign was purchased by the University of Helsinki in the year 2011 to be used in the research of biophysical characteristics of vegetation dynamics, ecology, forestry and agriculture. The specifications for the sensor with the configurations it was used with in this campaign are given in Table 1.

Table 1. Specification for AisaEAGLE sensor with the configurations that were used in this campaign (Specim 2012; Kataja 2012).

Numerical aperture	F/2.4	FOV	37.7° (full)
Spectral range	400 – 1000 nm	Spatial pixels	1024 (total)
FWHM	3.3 nm (true)	FODIS	55 (pixels)
Spectral binning	8	Frame rate	120 Hz (planned)
Spectral sampling	8.64 – 9.55 nm	Pixel size	0.6 m (planned)
Number of bands	64 (8 * bin)	Radiometric res.	12 bits digital

AisaEAGLE was mounted at the bottom of a Cessna 208B Caravan I aircraft (Figure 6) of Department of Resource Surveys and Remote Sensing (DRSRS) that works under the Ministry of Mining of Kenya. Nikon D3X digital camera was installed for high spatial resolution mapping. The aircraft have been made for the use of aerial survey and it had an opening in the bottom. Mounting platform for the sensors was made of thick plywood plate specifically for this setup.

Figure 6. Cessna 208B Caravan I aircraft used in the campaign (left) and AisaEAGLE and Nikon D3X sensors mounted on the bottom of the aircraft. Images are taken by Tuure Takala and Pekka Hurskainen.

Raw data from AisaEAGLE sensor is stored as 12 bits binary stream in ENVI BIL (Band Interleaved by Line) format (Specim 2012; Figure 7). In BIL format the first line of the first band is followed by the first line of the second band until the first line is stored on all bands. Next the second line is stored on all bands etc. (RSI 2004). Each line consists of 1024 pixels. 55 of these pixels contain the FODIS (Fibre Optic Downwelling Irradiance Sensor) data that appears as thin black line on the left side of the images (Figure 8). FODIS sensor is attached to the same CCD as AisaEAGLE and measures the solar irradiance. It was located at the top of the aircraft (Specim 2012; Homolova et al. 2009). These values can be used in CaliGeo (Specim 2009) to calculate FODIS-ratio that is the recorded target radiance divided by the FODIS measurement. CaliGeo is a program provided by the sensor manufacturer for the radiometric correction of the data (Specim 2009). Dark current data is stored after each flight line and is seen as a black line in the bottom of each image (Figure 8). Dark current stores the noise caused by thermal electors generated by the sensor as it warms up. The raw files are in internal geometry and have no coordinate system. The 12 bit raw DN values are directly proportional to the electric current generated by the incoming photons hitting the CCD (Charge-Coupled Device) of the sensor (Figure 7). The values run from longer wavelengths on the left to the shorter wavelengths on the right. Each raw data file is accompanied with ENVI format header file that contains general information such as start and stop time of the sensor and coordinates for each image. Navigation files produced by Oxford RT3100 GPS/IMU (Oxford Technical Solutions 2007) unit store the position and attitude information for each line of data. AisaEAGLE was used in spectral binning mode 8. In this mode 8 adjacent bands (rows in the CCD) are stored as a single measurement. This gives better signal but the number of output bands is limited to 64.

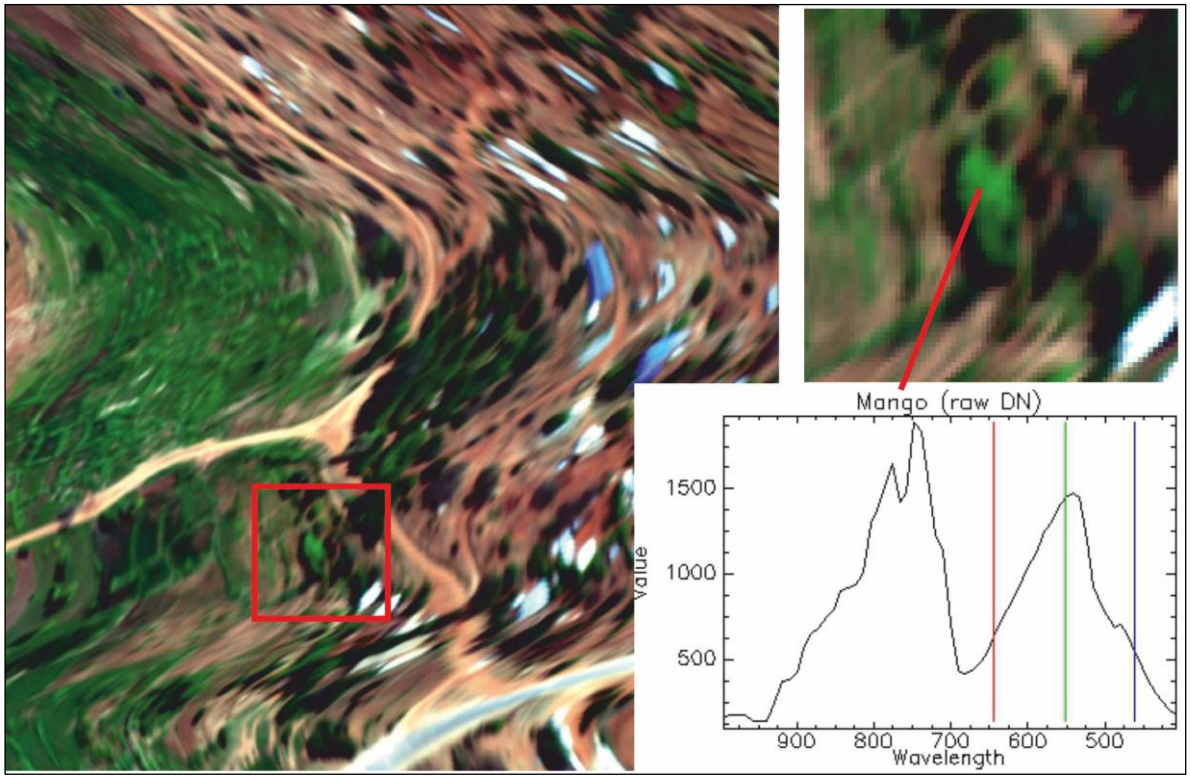

Figure 7. Example of AisaEAGLE raw data from plot 25 with spectra from a known mango tree in raw DN values.

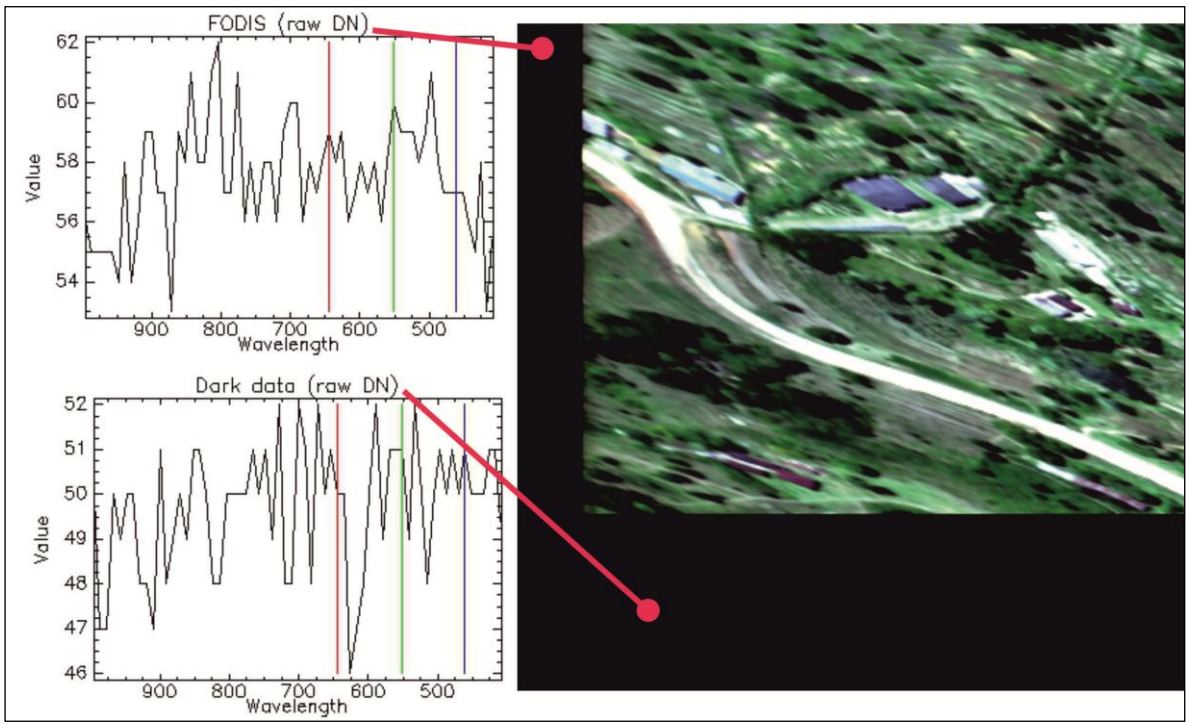

Figure 8. Example of FODIS and dark current spectra stored in AisaEAGLE raw data.

4.2 Flight campaign

Flight campaign in the Taita Hills was conducted in the period of mid-January to early February in 2012. This time period was chosen for relatively dry and cloud free weather conditions required by the AisaEAGLE sensor. The goal of the campaign was to cover the CHIESA main transect (Figure 5) with AisaEAGLE imaging spectrometer. Flight planning was done with NavCam software (MosaicMill 2014), which was also used for navigating the aircraft during the campaign. Planned at-ground pixel size for AisaEAGLE was 0.6 meters. AisaEAGLE uses pushbrooming technology and records frames continuously. Thus the flight planning was based on the speed of the aircraft, used frame rate, FOV and number of pixels along spatial axis of the sensor CCD.

Spatial resolution in across the flight path direction is defined by the flight altitude (Figure 9). Flight altitude (h) is calculated from FOV and swath (s). Swath equals to the number of spatial pixels (p_n) times the planned pixel size (p_s):

$$s = p_n * p_s$$

Each row has 1024 pixels of which 55 are used by FODIS. This means that 55 pixels need to be taken out from the calculations from both sides of the spatial axis so that the planning is done with equal opening angles on both sides. The planned swath is then calculated as 914 pixels * 0.6 meter pixel size which equals to 548.4 meter. Swath is divided by two to get the opposing cathetus for the flight altitude calculation. Flight altitude is the adjacent cathetus and tangent value is FOV divided by two. The flight altitude is then calculated:

$$h = \frac{\left(\frac{s}{2}\right)}{\tan\left(\frac{\mathrm{FOV}}{2}\right)}$$

Total FOV for 1024 spatial pixels is 37.36°. When 55 pixels are excluded from both sides of the remaining FOV is 34.58°. Based on the equation the correct flight altitude for 0.6 meter pixel resolution is 881.4 meters above ground level. Since there are elevation differences along the study transect the planning was made so that the flight altitude is 881.4 meters for the lowest point of each group of flight lines seen in Figure 9. This needs to be taken into account when the side overlap is calculated in NavCam. Side overlap is calculated automatically from ground elevation, FOV and above ground flight altitude. Lower areas will get higher side overlap and the pixel size will be the planned 0.6 meters.

Higher altitudes will have smaller side overlap and smaller nominal pixel size, which will be interpolated to 0.6 meters in radiometric correction.

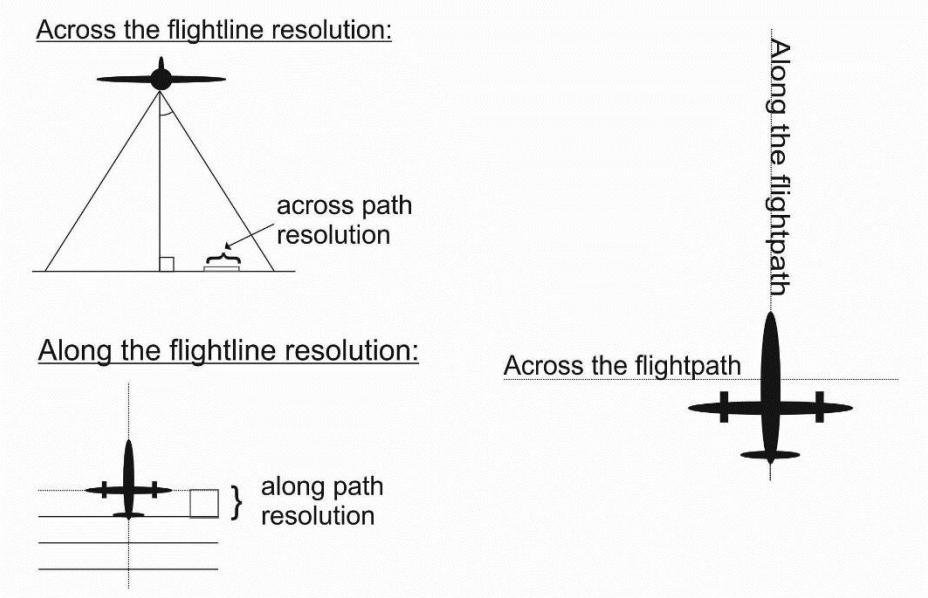

Figure 9. Visualization of across and along the flight path pixel resolution for pushbroom sensors.

Along the flight path pixel size for pushbrooming sensors is determined by the used frame rate and the speed of the aircraft. Lower flight speeds would give better signal as the sensor has more time to cover each pixel. Since keeping the aircraft stable in low speeds is difficult it was decided to use flight speed of 72 m/s which was suitable for Cessna 208B Caravan I aircraft type. Frame rate (f_r) that needs to be used to achieve the planned pixel size (p_s) in certain speed (S) is calculated by dividing S with p_s. This means that the faster the aircraft is moving more frequently a frame needs to be recorded to achieve the same pixel size.

$$f_r = \frac{S}{p_s}$$

Thus the f_r that needs to be used when S = 72 m/s to achieve p_s of 0.6 in the along the flight path direction is 120 Hz.

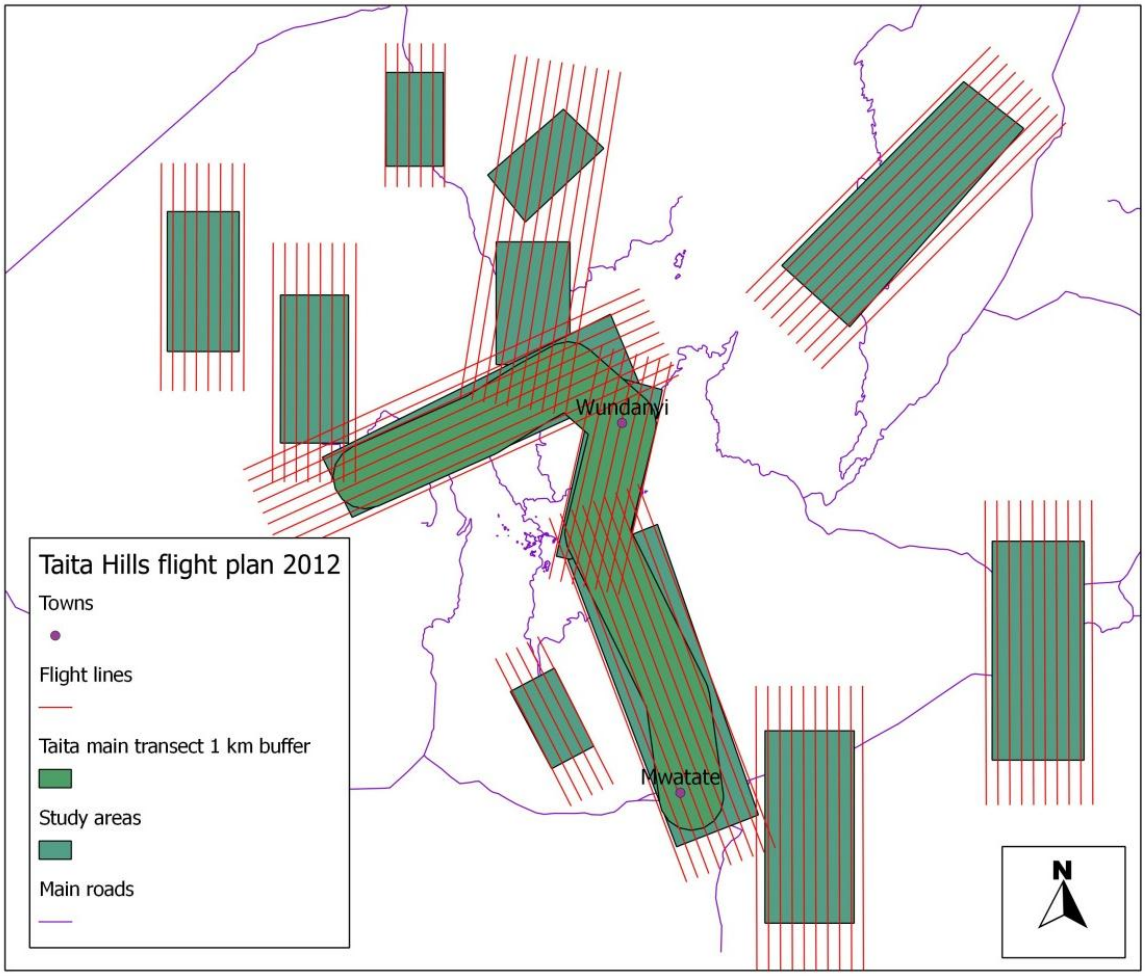

Figure 10. Flight plan for the flight campaign carried out in the Taita Hills in late January to early February in year 2012 (MosaicMill 2014). Taita main transect was covered for the CHIESA project. Other study areas marked with light green are used in other studies.

4.3 Study plots and vegetation maps

25 study plots covering an area of 100 * 100 meters were planned along the study transect for field mapping. The mapping was done in total for 21 plots until the field campaign ended. Plots were planned to locations where the agricultural crops were expected to be found. Accessibility was considered and all the plots were planned near a road that is accessible by a car. Five of these plots were located in the study area (Figure 11). The actual field mappings have varying areas as the interesting plant species were mapped also outside the study plots to gather more reference material. Four of the study plots are located in the valley that is seen as bright green color in Figure 11. Plot 23 is located further to the west on drier area.

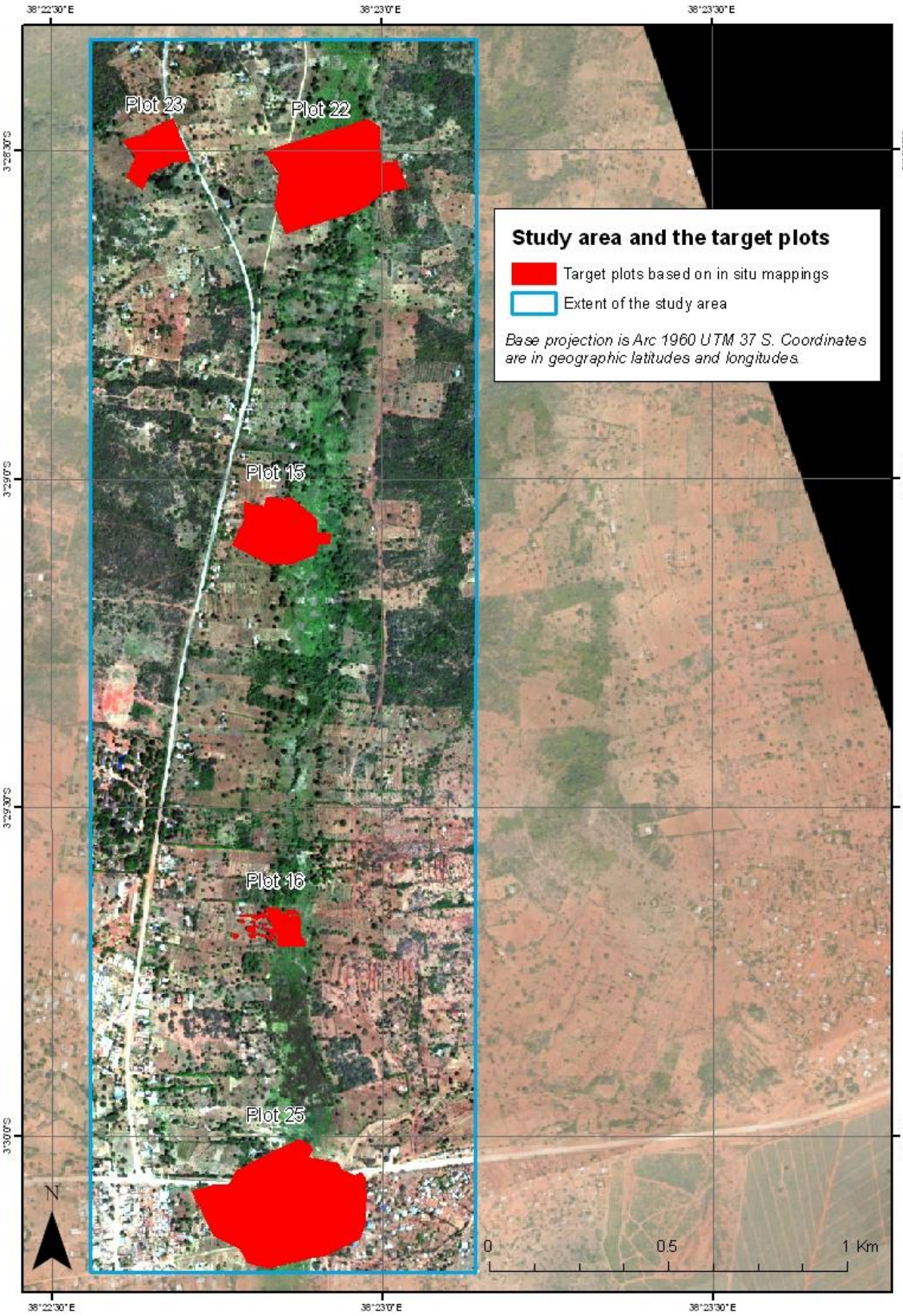

Figure 11. Study area and the mapped study plots on true color AisaEAGLE image. Basemap is aerial mosaic of Nikon D3X images acquired during the same campaign and processed by Pekka Hurskainen (CHIESA 2014).

Nikon D3X digital camera images were printed after the flights and were used for field mapping. For some study plots the new images were not available at the time of the field mapping and older images from the year 2006 were used. The mapping was done mainly by local guides as they had the best knowledge of the plant species found in the study area. Plant species were marked on paper maps that were later digitized using ArcMap 10.1 (Figure 12: appendix 1; ESRI 2011). Many polygons consist of a mixture of different plant species. The polygons are named after the dominant species with emphasis on the agricultural crops. For example large fields of maize may contain shrubs and other species but they are all marked as maize.

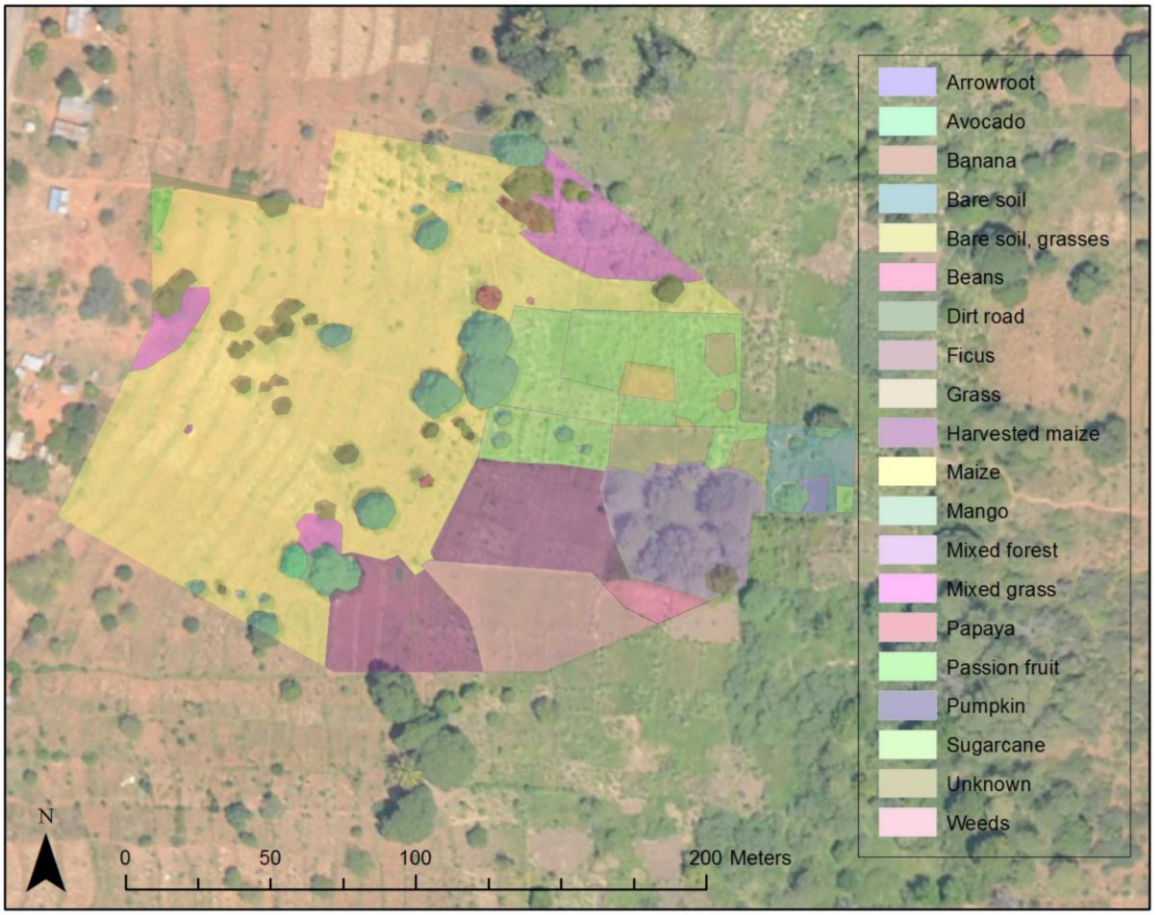

Figure 12. Plant species mapped from study plot 15. Polygons were digitized based on the paper maps on top of the Nikon 3DX image mosaic.

5. METHODS

5.1 Preprocessing of AisaEAGLE data

5.1.1 Radiometric correction

Radiometric correction of the AisaEAGLE raw data files was done with CaliGeo 4.9.15 software that is used exclusively with AISA sensor family for this purpose (Specim 2009). In radiometric correction procedure the sensor related sources of error and noise are removed based on laboratory calibrations and dark currents measurements. The general concept of the correction is described in Figure 13.

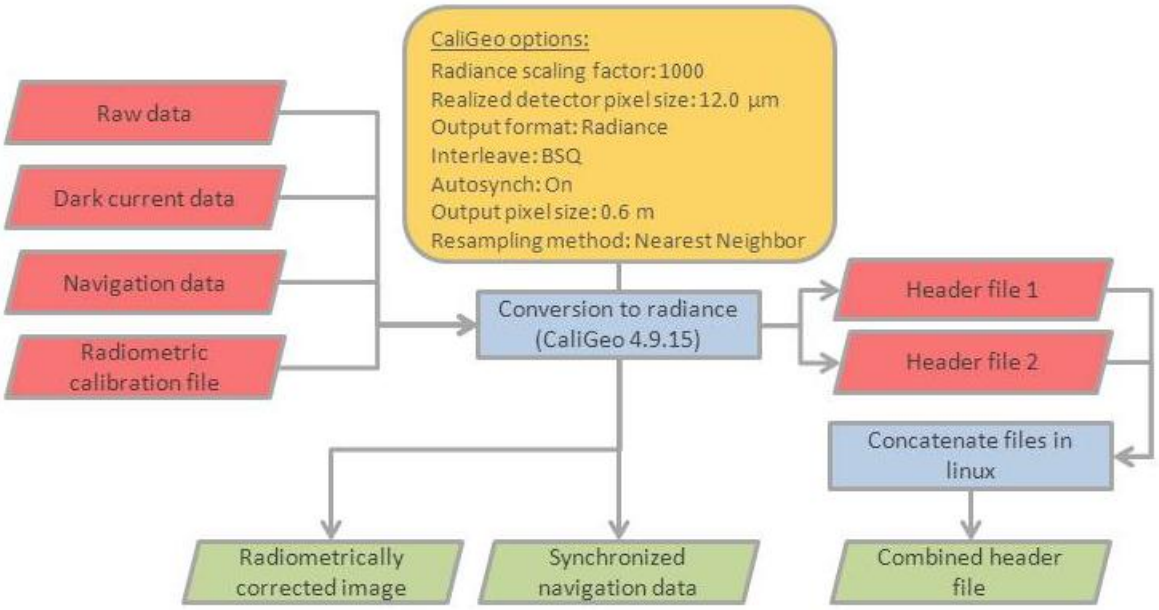

Figure 13. Flow chart of the radiometric correction procedure.

Dark current measurements were done after each flight line by closing the shutter while the sensor continued recording. The stored values are caused by thermal electrons that are generated by the sensor itself as it warms up. The average of these values on each band is reduced from the corresponding image bands. FODIS values are excluded at this point from further processing. Central wavelengths and spectral sampling values were implemented for each band based on radiometric calibration file provided by Specim.

The 12-bit DN values were converted to at-sensor spectral radiance values $L_{at\text{-}sensor}(\lambda)$. The values were multiplied by 1000 and stored as integer values to avoid data loss and simplify the further processing. The exact conversion algorithm of DN-values to spectral radiances

was not available, but the basic principal is the same as with other sensors. For ASTER data the conversion is done as following (Yarbrough et al. 2005):

$$L_{at-sensor}(\lambda) = C_{\lambda m}\ (\mathrm{DN}_{\lambda m}\ - 1)$$

Where $C_{\lambda m}$ is band and gain specific conversion coefficient and $\mathrm{DN}_{\lambda m}$ is the digital number of a particular band for a given gain and product version.

The wavelength axis was reversed to run from the shorter wavelengths on the left to the longer wavelengths on the right (Figure 14). Navigation data was interpolated to match each AisaEAGLE image row and stored in ASCII format. Oxford RT3100 has update rate of 100 Hz (Oxford Technical Solutions 2007) and AisaEAGLE was used with 120 Hz frame rate in this campaign. This means that the resulting location for each image row is an estimation based on the closest two time stamps from Oxford RT3100.

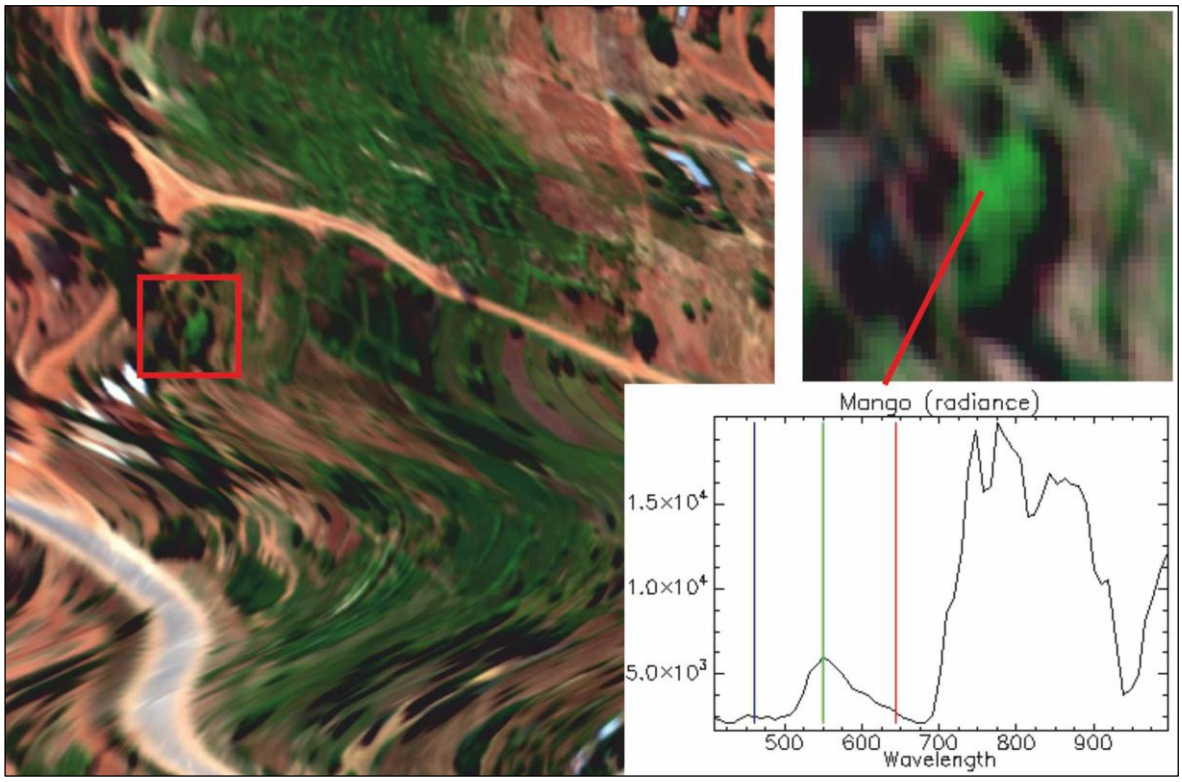

Figure 14. Example of the radiometrically corrected AisaEAGLE data with spectra of a known mango tree in at-sensor spectral radiance values.

5.1.2 Boresight calibration

Boresight calibration is a method to correct the difference between the orientations of Oxford RT3100 and AisaEAGLE sensor. These offsets will cause distortions in the georeferenced images if not corrected. Boresight parameters are indicated as the angular difference between the orientations of Oxford and AISA units as shown in Figure 15. These values can be calculated in Parge software that is used in geometric correction phase (Schläpfer 2011) by comparing points on the AisaEAGLE data to known points on a reference map. This method could not be used since there were no accurate reference maps of the study area available. CaliGeo software (Specim 2009) has an option to calculate the boresight parameters from three overlapping image lines. These lines were flown for this campaign near the town of Voi, where topography is flat and the resulting data is suitable for the correction. This method could not be used since the algorithm in CaliGeo was unable to take account of the missing 55 FODIS columns resulting in false values. Additionally the values calculated in CaliGeo and Parge are not equivalent to each other. The polarities are different and Parge calculates heading offset while CaliGeo calculates yaw offset. For these reasons the values used in this campaign are the same that were calculated by Tuure Takala in Parge for an earlier campaign in Hyytiälä, Finland in the summer of 2011. The used values were: roll 0.282, pitch 0.228, heading 0.480.

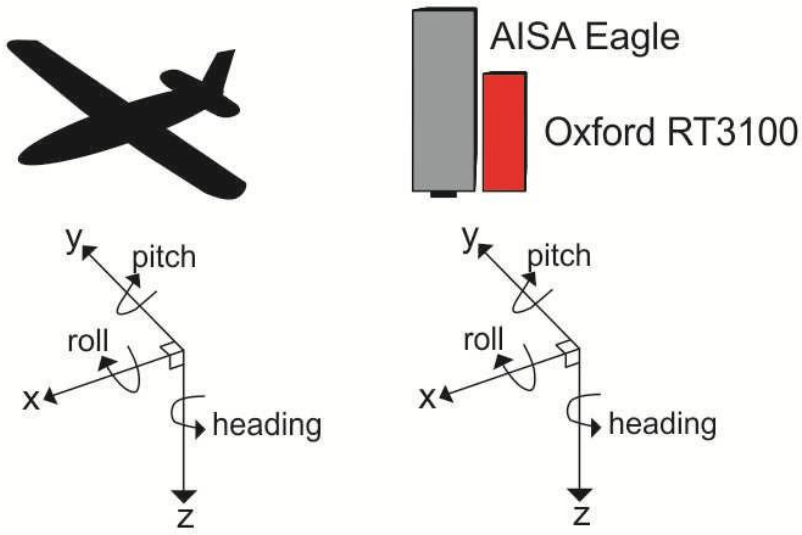

Figure 15. Visualization of the attitude directions (left) and offset angles between AisaEAGLE sensor and Oxford RT3100 (right).

5.1.3 Geometric correction

Geometric correction was done with Parge software (Schläpfer 2011). Parge constructs georeferenced images from the radiometrically corrected image in raw geometry, sensor model, navigation file and ground elevation data. The input files are radiometrically corrected AisaEAGLE image, interpolated navigation data in ASCII format, boresight values, sensor model and DEM. Sensor model contains across the flight path pixel number and position from the nadir in radians. This information was provided by Specim. The values are calculated from the used focal length and opening angle as a linear fit. DEM was provided by Pellikka et al. (2005). It was interpolated from 50-feet interval contour lines that were capture from Survey of Kenya 1:50 000 topographic paper map sheets. The resulting DEM has 20 meter planimetric resolution. The planimetric accuracy of this DEM is +/- 50 meters and altimetric accuracy 8 meters. The DEM was further interpolated to the target resolution of 0.6 meters.

There was a misconfiguration in OxfordRT3100 options during this campaign and the flight altitude information was stored in EGM96 geoidal heights instead of heights from the WGS84 reference plane. The elevation difference between these two reference systems is around 20–30 meters in the study area. The problem was solved by using arbitrary projection defined in Parge (Table 2) and adding 20 meter pseudo elevation value to the used DEM to compensate the difference.

Table 2. Projection and coordinate system specifications used with the georeferenced AisaEAGLE images.

Projection type:	Transverse Mercator	Center longitude:	39
Ellipsoid Datum:	Clarke 1880	Center latitude:	0
Semimajor axis:	6378249.145	False easting:	500000
Semiminor axis:	6356514.87	False northing:	10000000
Mercator scale:	0.9996		

The output from geometric correction is seen in Figure 16. The image is now transformed from internal geometry to a reference plane and it has coordinates for each pixel. The distortions seen in earlier images (Figure 14; Figure 7) are now corrected. The pixel values stay the same and are stored as $L_{at\text{-}sensor}(\lambda)$.

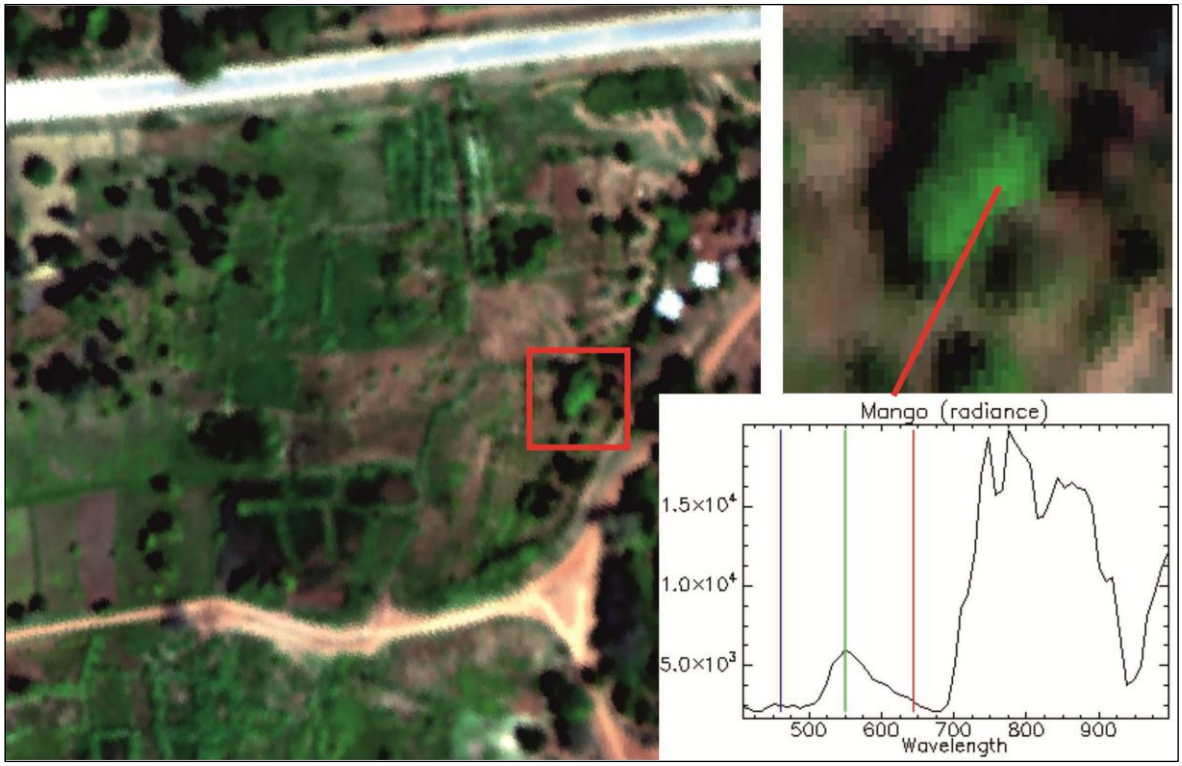

Figure 16. Example of the geometrically corrected AisaEAGLE data with spectra of a known mango tree in at-sensor spectral radiance values.

5.1.4 Atmospheric correction

Atmospheric correction of the geometrically corrected AisaEAGLE image was done with ATCOR-4 (Richter & Schläpfer 2011). ATCOR-4 is physically based atmospheric correction program for airborne and spaceborne imagery. It uses MODTRAN (moderate resolution atmospheric transmission) code as the basis of the radiative transfer calculations. The correction was done in flat ground mode where ATCOR-4 assumes that target surface area has Lambertian reflectance properties. The workflow of the correction is described in Figure 17. The input files for the correction are geometrically corrected AisaEAGLE image, sensor model and atmospheric file. Additionally the correction needs time of the image capture, coordinates, ground elevation, flight altitude, heading, solar zenith and solar azimuth for each flight line.

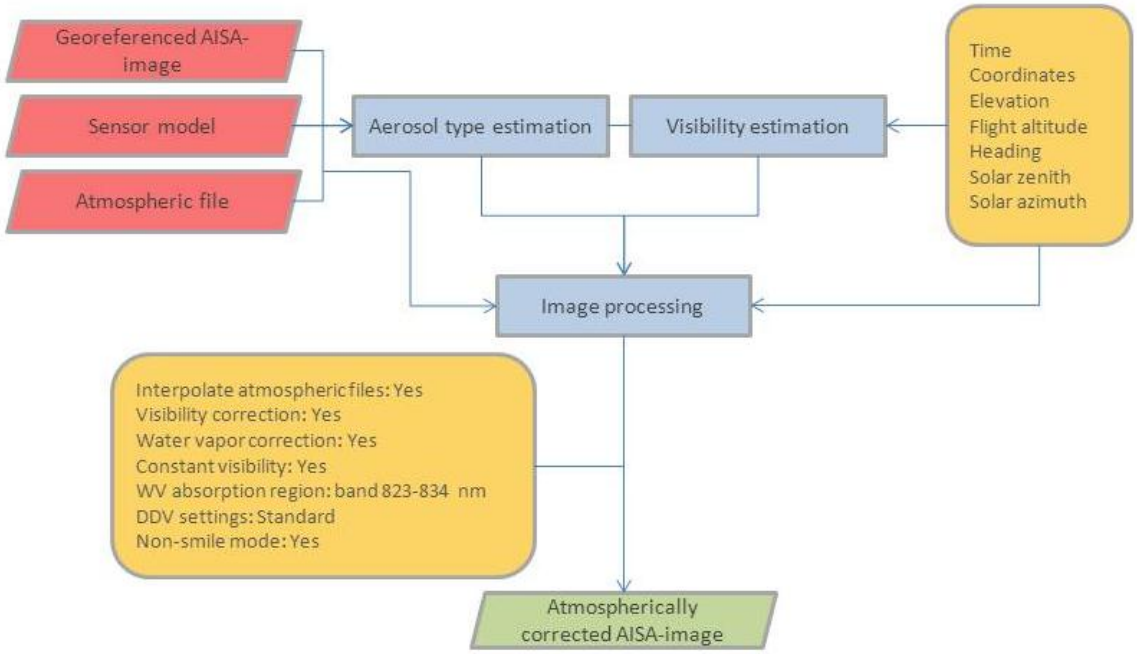

Figure 17. Workflow of the atmospheric correction based on ATCOR-4 manual (Richter & Schläpfer 2011).

The sensor model was created in ATCOR-4 from unrectified AisaEAGLE image. The model was configured to have FOV of 34.58 degrees, 969 across track pixels and radiance scaling factor of 1000. These values need to match the AisaEAGLE image specification after the FODIS pixels are ignored in the radiometric correction. Smile sensor response type was set to fourth order butterworth with close to rectangular frequency response type. This is the recommended response type for AisaEAGLE data when it is used in spectral binning mode 8. Spectral sampling values are stored in the ENVI header file. Spectral response curves were generated from these values and center wavelengths by fitting them to the fourth order butterworth frequency response type. The resulting channel filter files (Figure 19) are approximations of how the incoming radiation is hitting each pixel in the CCD (charge coupled device) of the sensor. Spectral sampling values were used instead of FWHM (full width at half maximum) values as these were stored in the header files. The true FWHM values have more variance than the spectral sampling values as seen in Figure 18.

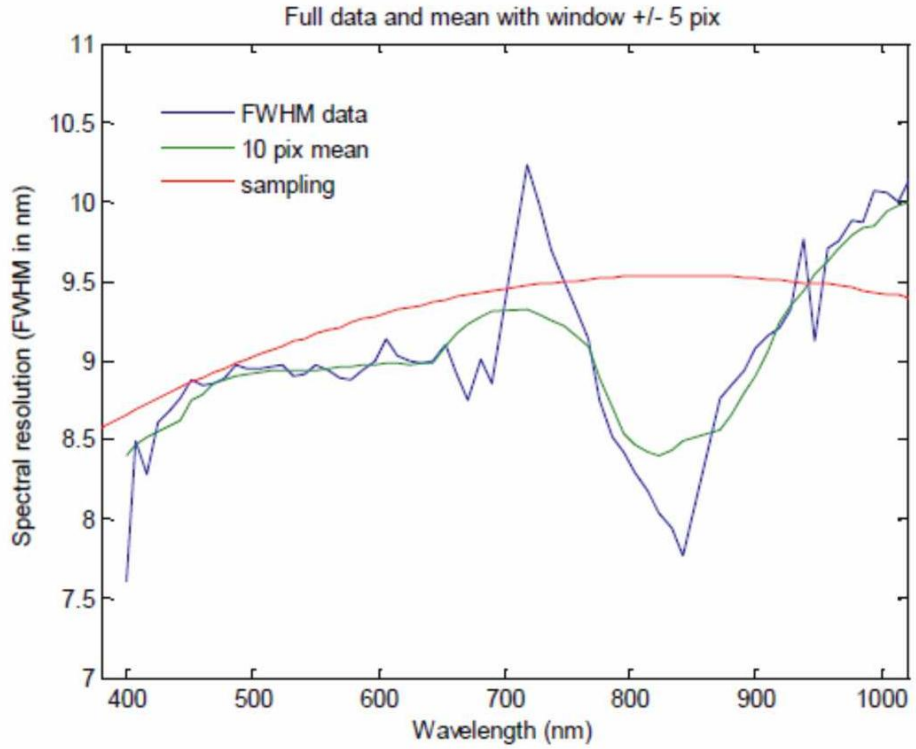

Figure 18. Spectral resolution measurements of AisaEAGLE sensor with spectral binning value 8. The values are FWHM based on laboratory measurements, 10 pixel mean of the FWHM and spectral sampling values that were used in the processing of this data (Kataja 2012

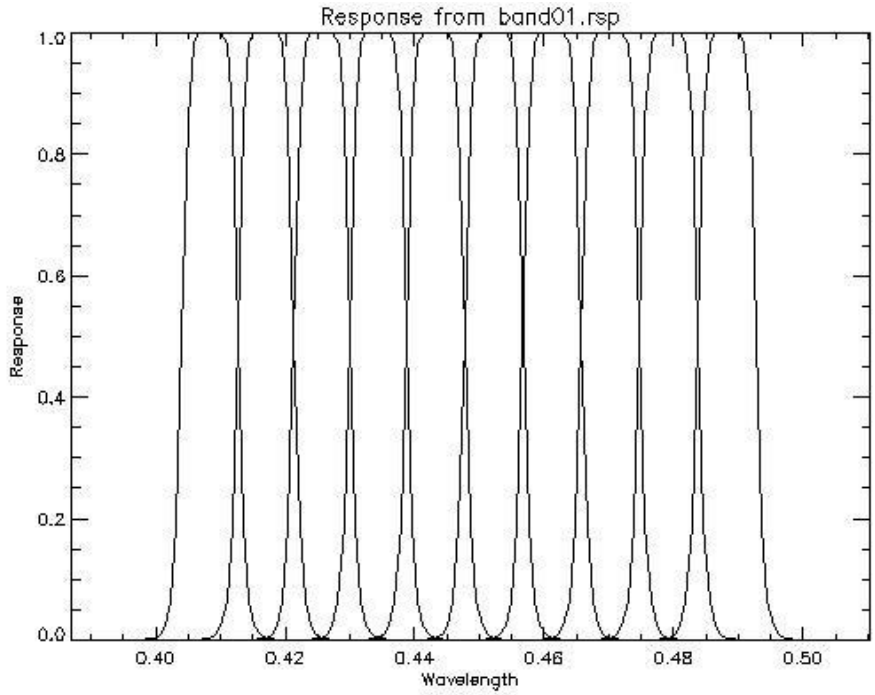

Figure 19. Spectral response curves for 10 first AisaEAGLE bands calculated in ATCOR-4 (Richter & Schläpfer 2011).

The atmospheric file was created separately for each flight line from approximated water vapor content in the atmosphere, aerosol model type and the flight altitude. Water vapor amount was estimated in ATCOR-4 spectra mode where different input parameters can be tried on individual pixels. Based on these tests the average water vapor was set to 2.9 grams of water per cm^2 from ground level to top of the atmosphere. Aerosol type was estimated with aerosol type function that suggested maritime aerosol model. Study area is not located near large water bodies so the second highest recommendation, rural aerosol model, was used (Figure 20). Average flight altitude was calculated for each flight line by calculating the average of the altitudes stored in navigation files. Atmospheric model was used as preliminary input for the atmospheric correction procedure.

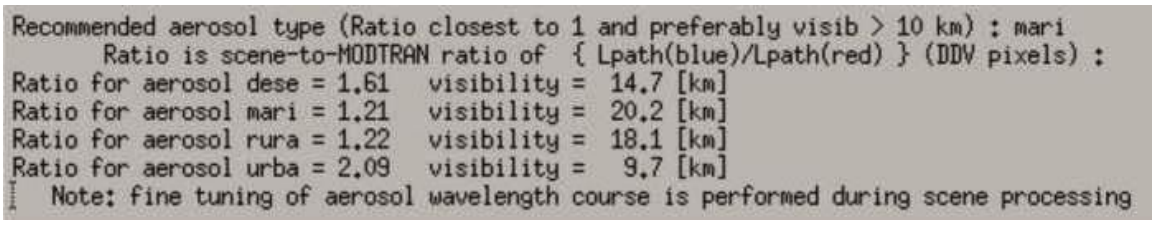

Figure 20. Results of the aerosol type function in ATCOR-4. Rural aerosol model was second highest recommendation and was used in the processing (Richter & Schläpfer 2011).

Solar zenith and azimuth angles were calculated for each flight line with ATCOR-4 solar calculator. Solar zenith is located directly above the target on a straight line from the center of the earth through the target. Solar zenith angle is the angle from solar zenith to the sun when target is the origin. Solar azimuth angle is the angle from geographic north to the sun on a reference plane that is projected perpendicular to the target zenith (Jensen 2000: 348–350). Solar calculator calculates these values from UTC time and geographic coordinates. UTC time for each flight line was calculated by averaging the sensor start and stop time stored in the header files. Geographic coordinates for each line were calculated by averaging the start and stop coordinates. Flight heading and altitude for each flight line were calculated as the averages of the values stored in navigation files. Scene elevations were calculated as the averages of the DEMs that were cut down to cover individual flight lines. Estimated visibility is the value given by ATCOR-4 aerosol type function for rural model (Figure 20).

Image processing was done separately for each flight line. First step was to calculate interpolated atmospheric files for the average flight altitudes. Next the atmospheric correction options were defined. In this case the aerosol optical thickness and water vapor

corrections were chosen. ATCOR-4 corrects the water vapor absorption by comparing the absorption regions of 823.3 to 833.9 nm (bands 46 and 47) to the adjacent non absorbing regions of 795.2 and 842.9 nm (bands 43 and 48). The values are the center wavelengths of these bands in AisaEAGLE data. Linear band regression option was used to reduce noise. Aerosol optical thickness was corrected by calculating visibility index based on DDV (dark dense vegetation) reference pixels that were collected from each image. DDV pixels are vegetation targets that have high reflectance in NIR region and strong absorption in red region. The process assumes average clear atmospheric condition (visibility 25 km) to calculate the surface reflectance for these bands before the pixels can be selected. DDV pixels need to fulfill the following conditions:

$$\frac{\rho_{\mathrm{nir}}}{\rho_{\mathrm{red}}} \geq 3 \text{ and } 0.10 \leq \rho_{\mathrm{nir}} \leq 0.25 \text{ and } \rho_{\mathrm{red}} \leq 0.04$$

Where ρ_{nir} surface reflectance in near infrared (843 nm) and ρ_{red} is surface reflectance in red (663 nm). Condition $\rho_{\mathrm{nir}} \geq 0.10$ excludes water pixels while all the conditions combined exclude soil pixels. This algorithm runs iteratively until at least 5% of pixels are defined as DDV. After each iteration the ρ_{red} threshold is decreased in steps of 0.005 down to 0.025. Average visibility of the reference pixels is calculated and used to fill the gaps in the optical thickness map (visibility). Additionally surface reflectance in red band is calculated as a fraction α of the NIR band reflectance:

$$\rho_{\mathrm{red}} = \alpha * \rho_{\mathrm{nir}}$$

Where α = 0.1 is an average empirical value yielding results in close agreement with other methods. These values and DDV pixels are used with MODTRAN code to calculate the visibility index. The details are found in ATCOR-4 manual (Richter & Schläpfer 2011: 164). Spectral smile correction was not applied. Spectral smile effect is caused by aberrations in the imaging optics of the sensor as the light that enters the sensor through entrance slit and is scattered according to wavelength is not perfectly projected on the detector grid of the sensor (Ceamanos & Douté 2009). This causes a shift in the central wavelength of light on a given band across the spatial axis of the detector grid. This effect is sensor specific and can be calculated from images that are in internal geometry. As the atmospheric correction was applied to geometrically corrected images the smile correction was not done. After all these parameters are set the atmospheric correction can be applied for the images. Example of the corrected spectra is seen in Figure 21.

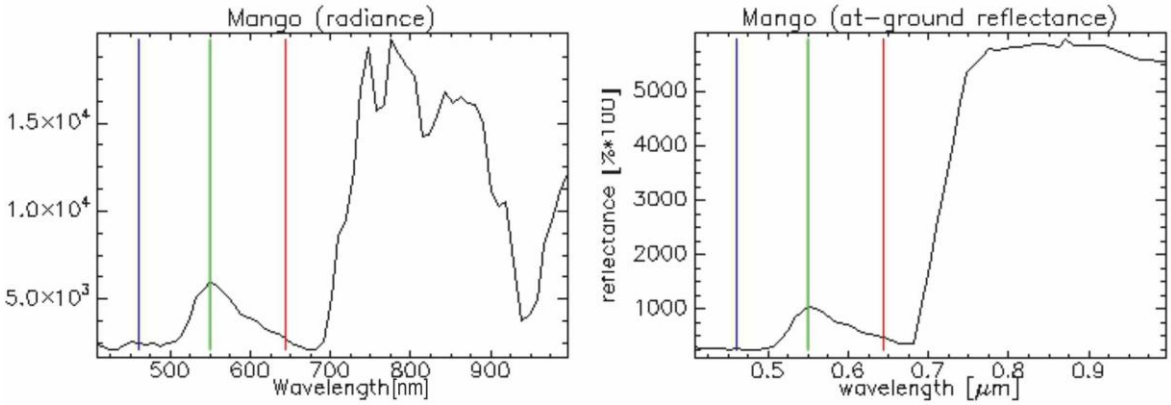

Figure 21. Spectra of known mango tree in at-sensor radiance values before atmospheric correction (left) and the same target in at-ground reflectance values after the correction.

5.2 MNF transformation

5.2.1 Functionality of the MNF transformation

Minimum noise fraction (MNF) transformation (Green et al. 1988) is used to segregate noise in the data, to reduce the number of spectral bands and to determine the inherent dimensionality of the data. MNF transformation as implemented in ENVI is based on two cascading PCA transformations (RSI 2004). First PCA is based on estimated noise covariance matrix. It decorrelates and rescales the noise in the data. The result is data where noise has unit variance and no band-to-band correlations. Second transformation is a standard PCA transformation that creates n number of new bands where n_{max} is the number of input bands. Signal-to-noise ratio (SNR) is maximized in the first band and decreases towards the last bands (Canty 2010). This means that the majority of the useful information is packed in the first bands and last bands contain primarily noise (RSI 2004; Petropoulos et al. 2012). The inherent dimensionality of the AisaEAGLE data after the transformation is the number of bands that can hold the whole spectral information content of the input data (Schlamm et al. 2009). Other bands contain mainly noise and are left out of the further processing steps.

5.2.2 Finding optimal MNF bands for SVM classification

MNF transformation was applied to the atmospherically corrected AisaEAGLE image and the resulting bands were analyzed. The optimal number of MNF bands was searched primarily by analyzing the eigenvalues of the bands (Figure 28) and the visual appearance of the single band black and white images (Figure 30). ENVI manual states that the bands that have eigenvalues close to one contain primarily noise and should be left out (RSI

2004: 685). There should be a sudden break in the slope depicting the eigenvalues for each band. The values that are above this curve should be used. To further analyze the information content in the bands Local Moran's I index was calculated for the bands (Figure 29). This index identifies the clustering of bands that have similar values with surrounding pixels. The index was calculated based on Rook's Case neighborhood rule where each central pixel is compared to the pixels on the top, bottom, left and right. Values close to 1 indicate strong clustering of similar values and negative values no clustering. The same index was calculated for reflectance image that was used for reference (RSI 2004).

5.2.3 The impact of MNF transformation on the classification accuracy

The impact of MNF transformation on the classification accuracy was assessed by comparing the confusion matrices of two SVM classifications. First the classification was done on AisaEAGLE data with 64 bands in reflectance values covering the whole study area (Table 10). The second classification was done on the same extent with data that used first 20 bands of the MNF transformed data (Table 11). Probability threshold was set to 0.00 and penalty parameter to 100 for both classifications. Gamma values that were used were the default values given by ENVI. Default gamma value for 64 band reflectance image was 0.016 and for 20 band MNF image 0.05. Training and testing samples are listed in Table 4.

5.3 SVM classification

5.3.1 Functionality and parameters of SVM classifier

Support vector machine (SVM) is parametric machine learning algorithm introduced to wider public in the 1990's. It is based on statistical learning theory developed by Vladimir Vapnik in the 1960's. Many other people have also participated in the development of the algorithm during the years (Vapnik 1998; Boser et al. 1992). In statistical learning theory a classifier learns from input training samples with known identity and predicts the outcome of data points with unknown identity (Pal & Watanachaturaporn 2004). SVM aims to minimize the upper bound on the expected error over the whole dataset. This is called structural risk minimization. SVM classifier locates an optimal separating hyperplane (Figure 22) that maximizes the distance between the closest training sample from each class and the separating hyperplane (Melgani & Bruzzone 2004). Training samples that are closest to the optimal separating hyperplane are called support vectors. If the optimal separating hyperplane is not able to classify input data without error the data is transformed

to a higher dimensional space using different kernels that will spread the data in a way that the optimal separating hyperplane may be found (Pal & Watanachaturaporn 2004).

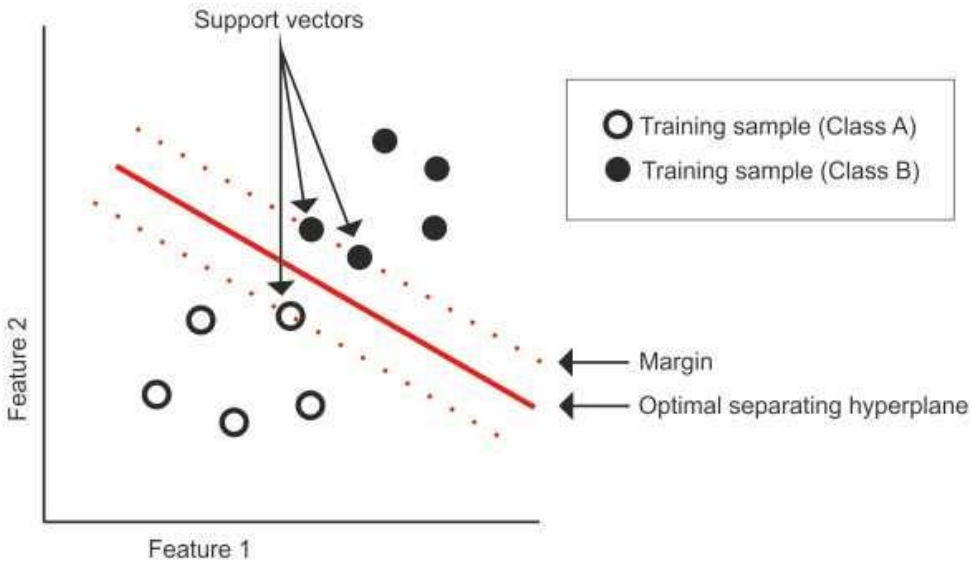

Figure 22. Example of binary class linearly separable classification problem solved with SVM classifier based on work by Melgani & Bruzzone (2004).

For example if the classification problem has two classes then the algorithm learns from a given set of k training samples, $(x_i, y_i),\ldots, (x_k, y_k)$, $x_i \in \mathrm{R}^N$, $y_i \in \{-1, +1\}$, which are drawn from a fixed but unknown cumulative (probability) distribution function $P(x,y)$, where x is an N-dimensional observed data vector, y_i is a class label and R is the set of all real numbers. A decision rule is represented by $\{f_\alpha(x) : \alpha \in \Lambda\}$, $f_\alpha : \mathrm{R}^N \rightarrow \{-1, +1\}$ where Λ is the set of parameters used in the decision rule. The aim is to assign class label y, based on the training samples x, and a decision rule f_α that provides the smallest possible expected risk defined as:

$$\mathrm{R}(\alpha) = \int L\big(y, f_\alpha(x)\big)\, dP(x,y)$$

The function f_α is called the hypothesis. The set $\{f_\alpha(x) : \alpha \in \Lambda\}$ is called the hypothesis space and $L(y, f_\alpha(x))$ is the loss of discrepancy between the response y of the teacher to a given input x and the response $f_\alpha(x)$ provided by the learning machine. $P(x,y)$ is the cumulative distribution function. Further details on statistical learning theory are provided by Vapnik (1998).

In the simplest case the problem is linearly separable meaning that a separating hyperplane can be found that separates the two classes without error (Melgani & Bruzzone 2004). Training set is assumed to consist of N number of vectors from the *d*-dimensional feature space $x_i \in R^d$ ($i = 1,2,\ldots,N$) and target $y_i \in \{-1, +1\}$ is associated to each vector x_i. Since the classes are linearly separable it is possible to locate at least one linear hyperplane defined by vector $w \in R^d$ and bias $b \in R$ that separates the two classes without error. The membership decision rule is based on function sgn[$f(x)$], where $f(x)$ is the discriminant function associated with the hyperplane and defined as:

$$f(x) = w * x + b$$

Linearly separable classification problem with two classes is the simplest way to explain the functionality of the classifier, but in practice this is rarely the case. When the algorithm is applied to remote sensing data it is normal that there are dozens of classes of interest. IF the problem is not linearly separable SVM classifier can transform the input data to higher dimensional feature space (Figure 23) using a variety of kernels (K) for the transformation where the optimal linear hyperplane can be located. ENVI software provides four possible kernel types (ENVI support 2014). The simple linear kernel is showed as an example together with RBF (Radial Basis Function) kernel, which is known to give good results vegetation classifications based on hyperspectral data (Petropoulos et al. 2012; Roli & Fumera 2001; Melgani & Bruzzone 2004).

Linear: $K(x_i, x_j) = x_i^t x_j$

RBF: $K(x_i x_j) = \exp\left(-g \left|\left|x_i - x_j\right|\right|^2\right), g > 0$

Where g is the gamma term. Gamma is a user defined value that is used to control the transformation. Default value in ENVI is the inverse of the number of input classes (ENVI support 2014; Petropoulos et al. 2012).

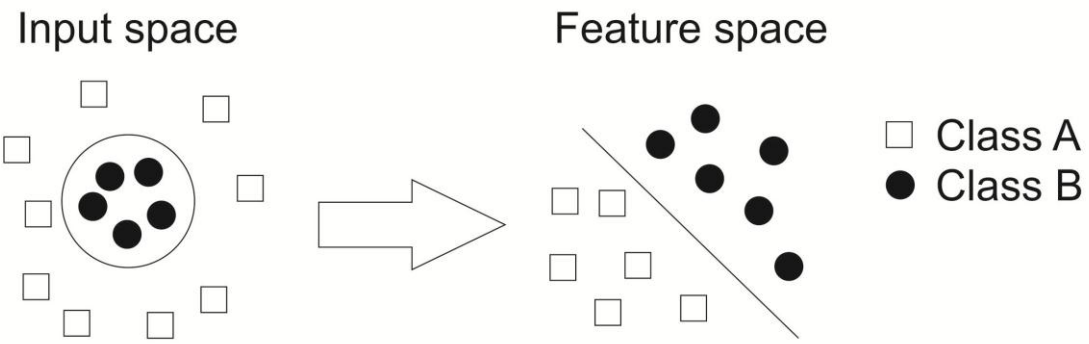

Figure 23. Transformation from linearly non-separable input space to linearly separable feature space based on the work by Pal & Watanachaturaporn (2004).

Soft margin classification was introduced to SVM classifier by Bennet & Mangasarian (1992) and Cortes & Vapnik (1995) (Pal & Watanachaturaporn 2004). This allows the control over the amount of allowed misclassifications and controls the trade-off between training errors and rigid margins. In ENVI this is controlled with user defined penalty parameter (ENVI help 2014). When this value is increased the cost of misclassifying points increases and the model is more accurate, but it does not generalize as well. Increasing this value also suppresses training data from jumping between classes as changes are made to other parameters.

In ENVI it is also possible to set probability threshold value that defines the probability limit that must be exceeded for a pixel to be classified. Pixels that have lower probabilities to belong to any of the classes than this value are left unclassified. If the value is set to 0 then all pixels are classified into one of the classes. If the value is 1 then the pixel need to have 100% probability to belong to one of the classes. Pyramid reclassification threshold can be used if it is not needed to do the classification on full resolution image. In this thesis all the classifications are done in full resolution.

5.3.2 Collecting training samples

SVM classifier applies the classification on the dataset based on training samples that are collected from the image that will be classified. These samples will form the classes that are seen as features in Figure 22. Samples were collected in two phases. First a smaller set of samples was collected from plot number 15 (Figure 12; Table 3). These samples were used to test how different parameters affect the classification result on a subset of the full image. After the parameters were found a new set of samples was collected from the 5

plots shown in Figure 11, Figure 12 and appendix 1. These samples (Table 4; appendix 2) were used for the classification of the full study area. The samples were divided to training and testing groups with IDL script provided by Matti Mõttus. The script gives random numbers between 0 and 1 to each sample and then assigns the samples with values less than 0.7 to training sample group and the rest to the testing sample group. Training sample group was used to apply the classification for the whole study area. Testing sample group was used with ENVI confusion matrix –tool (RSI 2004) to assess the accuracy of the classifications.

Table 3. Number of samples of known targets collected from study plot 15 for the parameter testing.

	Total
Maize	159
Sugarcane	190
Mango	125
Artificial	192
Baresoil	119

Table 4. Number of samples of known targets collected from 5 study plots for the classification of the whole study area.

	Total	Training	Testing
Banana	420	280	140
Maize	227	155	72
Mango	612	427	185
Sugarcane	927	689	238
Yam	306	202	104
Acasia	263	193	70
Grevillea	170	119	51
Building	640	435	205
Baresoil	637	443	194
Tarmac	611	431	180

The samples were collected with ENVI ROI-tool (RSI 2004). The possible input sample types were polygon, polyline or point vectors. In this case the most suitable type was point vectors, since they can be collected for individual pixels that are certain to belong to the target class (Figure 24). This was important since the aim was to classify single plants and for example individual maize might give a signature only from a single pixel. The fields were very heterogeneous as seen in Figure 12 and thus collecting polygons from a field would give very mixed spectral signals. The plant species were located in AisaEAGLE data by comparing it visually with the field maps (Figure 12: appendix 1). There were over 50 plant species mapped from the study plots. If the species was an agriculture crop and it had enough observations it was used in the classification. Only 5 agricultural crops and 2

tree species filled these requirements. Additionally samples were collected from building, bare soil and tarmac road targets to separate non-vegetation classes from the rest.

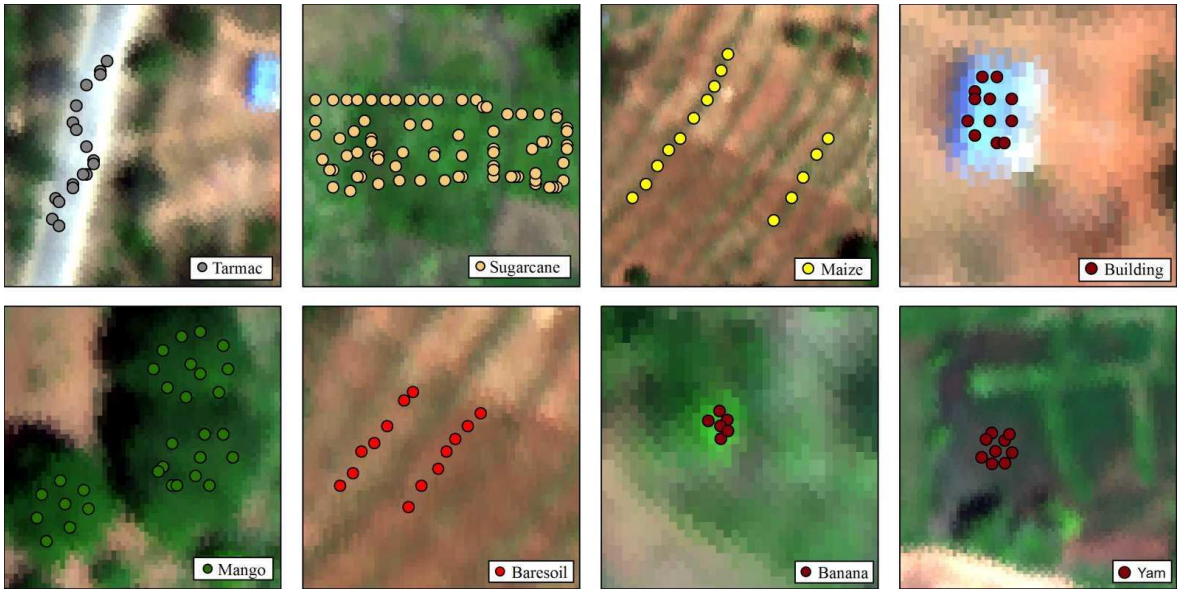

Figure 24. Examples of how the ground reference samples were collected with ENVI ROI-tool (RSI 2004).

5.3.3 Optimum parameters of the SVM classifier

SVM classifier is used with RBF kernel that was chosen based on good results in previous studies (Petropoulos et al. 2012; Roli & Fumera 2001; Melgani & Bruzzone 2004). Other parameters were searched by testing different combinations of these parameters. The tests were applied on a subset of plot 15 (Figure 12). MNF transformation was applied to the data before classification and only 20 first MNF bands were used. To keep the parameter search as simple as possible only five classes: maize, sugarcane, mango, artificial and bare soil were tested. The training samples that were used are listed in Table 3.

Gamma parameter was searched first (Figure 33). Tested values were 0.01, 0.05, 0.10, 0.50 and 100.00. During the tests penalty parameter was set to 100 and probability threshold to 0.50. The results were compared with ENVI change detection tool.

Penalty values 50, 100 and 500 were tested (Table 7; Table 8). Gamma value was set to 0.05 and probability threshold to 0.50 during the tests. The results were compared with ENVI change detection tool.

Probability threshold values of 0.00, 0.50, 0.75, 0.80, 0.85, 0.90, 0.95 and 0.99 were tested while gamma value was set to 0.05 and penalty value to 100 (Figure 35). Overall accuracy

(OA) and overall accuracy for classified pixels (OA_{cp}) were calculated for each classification. For these tests the testing samples were the same as the training samples and they are only used to analyze the impacts of the threshold values and do not represent the real accuracies of these classifications (Table 3). The classified images were assessed visually by analyzing the changes that happened for a known sugarcane field, an unknown tree and field of mixed grasses with different threshold values.

5.3.4 Crop classification of the study area with SVM classifier

Two crop classifications were done for the full study area (Figure 36). The classifications were applied on MNF transformed AisaEAGLE data that covered the full study area. Only first 20 MNF bands were used in the classification. Both classifications used RBF kernel with gamma value 0.05, penalty value 100 and pyramid threshold level 0. First classification was done with probability threshold value 0.00 and second classification with value 0.90. Agricultural crops that were classified are maize (*Zea*), sugarcane (*Saccharum*), yam (*Dioscorea*), banana (*Musa acuminate*) and mango (*Mangifera*). Additionally acacia (*Acacia*) and grevillea (*Grevillea*) trees were classified. The names in the brackets are the scientific names of the plant genus. Each genus contains many species, but in this case to all members of specific genus is referred by their common names (before brackets). For example there are many acacia species found in the study area and they are all referred to as acacias. Non-vegetation classes were building, tarmac and bare soil classes. These 10 classes are based on training samples (Table 4; appendix 2). Accuracy assessment of the classifications was done with testing samples that were independent from the training samples (Table 4).

5.4 Accuracy assessment with confusion matrices

Accuracy of the classifications is assessed with ENVI confusion matrix tool (RSI 2004; Raghuveer & Manoj 2004). Confusion matrices compare the testing group pixels to the same pixels in classified image. Various indexes are then calculated from these tables.

Overall accuracy (OA) is calculated by summing the number of correctly classified testing pixels (N_c) and dividing it by the total number of testing pixels (N).

$$\mathrm{OA} = \frac{N_c}{N}$$

OA indicates the overall accuracy of the whole image. However when the probability threshold is increased the number of pixels left unclassified increases. Thus it is

meaningful to calculate the accuracy for the classified pixels (OA_{cp}) only, where the number of unclassified pixels (U_P) is reduced from the total number of testing pixels (N).

$$\mathrm{OA_{cp}} = \frac{N_c}{(N - U_p)}$$

Overall accuracy excludes omission (EO) and commission errors (EC) from the assessment (Congalton 1991). Kappa coefficient (*K*) includes these and provides more precise measure for the general accuracy of the classification. It is calculated by multiplying the total number of pixels in all the testing classes (*N*) by the sum of the confusion matrix diagonals (x_{kk}), subtracting the sum of the testing pixels in a class times the sum of the classified pixels in that class summed over all classes, and dividing by the total number of pixels squared minus the sum of the testing pixels in that class times the sum of the classified pixels in that class summed over all classes.

$$K = \frac{N \sum_{\mathrm{k}} X_{kk} - \sum_k x_{k\Sigma}\, x_{k\Sigma}}{N^2 - \sum_k x_{k\Sigma}\, x_{k\Sigma}}$$

Producer accuracy (PA) is the ratio of correctly classified testing pixels (N_{ct}) to the total number of testing pixels in the same class (N_t).

$$\mathrm{PA} = \frac{\mathrm{N_{ct}}}{\mathrm{N_t}}$$

User accuracy (UA) is the ratio of correctly classified testing pixels (N_{ct}) to total number of testing pixels classified to the same class in the classified image (N_i).

$$\mathrm{UA} = \frac{\mathrm{N_{ct}}}{\mathrm{N_i}}$$

Error of commission (EC) is the ratio of pixels that are incorrectly classified to the class of interest (I_p) to the total number of pixels in the same class in the classified image (N_i).

$$\mathrm{EC} = \frac{\mathrm{I_p}}{\mathrm{N_i}}$$

Error of omission (EO) is the ratio of incorrectly classified testing pixels (I_t) to the total number of testing pixels in the same class (N_t).

$$\mathrm{EO} = \frac{\mathrm{I_t}}{\mathrm{N_t}}$$

6. RESULTS

6.1 Preprocessed AisaEAGLE data

The result of the preprocessing procedure of AisaEAGLE data was a georeferenced and atmospherically corrected data mosaic consisting of three overlapping flight lines that were cut down to the extension of the study area (appendix 2). There are around 3–5 meter distortions in the areas where two flight lines meet as seen from the mismatching roads in Figure 25.

Figure 25. Example of the quality of the mosaicked AisaEAGLE data.

The pixel values were atmospherically corrected and converted to at-ground reflectance values (Figure 26). All vegetation targets have low reflectance at 450 nm and higher values at 550 nm. At 650 nm the reflectance drops again for all other vegetation targets except maize and acacia. From 680 nm the reflectance increases rapidly until 750 nm. All other vegetation targets have the highest reflectance values at around 750 to 900 nm except maize. The reflectance for maize increases until 1000 nm. The reflectance values have greater variations within species after 750 nm. The lowest reflectance values for mango are around 20% and the highest over 60%. Standard deviation for mango is much lower than for other targets. All other vegetation targets except maize have a slight decrease in reflectance in 900 to 1000 nm region. The reflectance values for bare soil and tarmac road targets increase evenly from shorter wavelengths to longer wavelengths. Building targets have generally higher values in 450 nm than other targets and not have the clear increasing trend toward longer wavelengths as other targets.

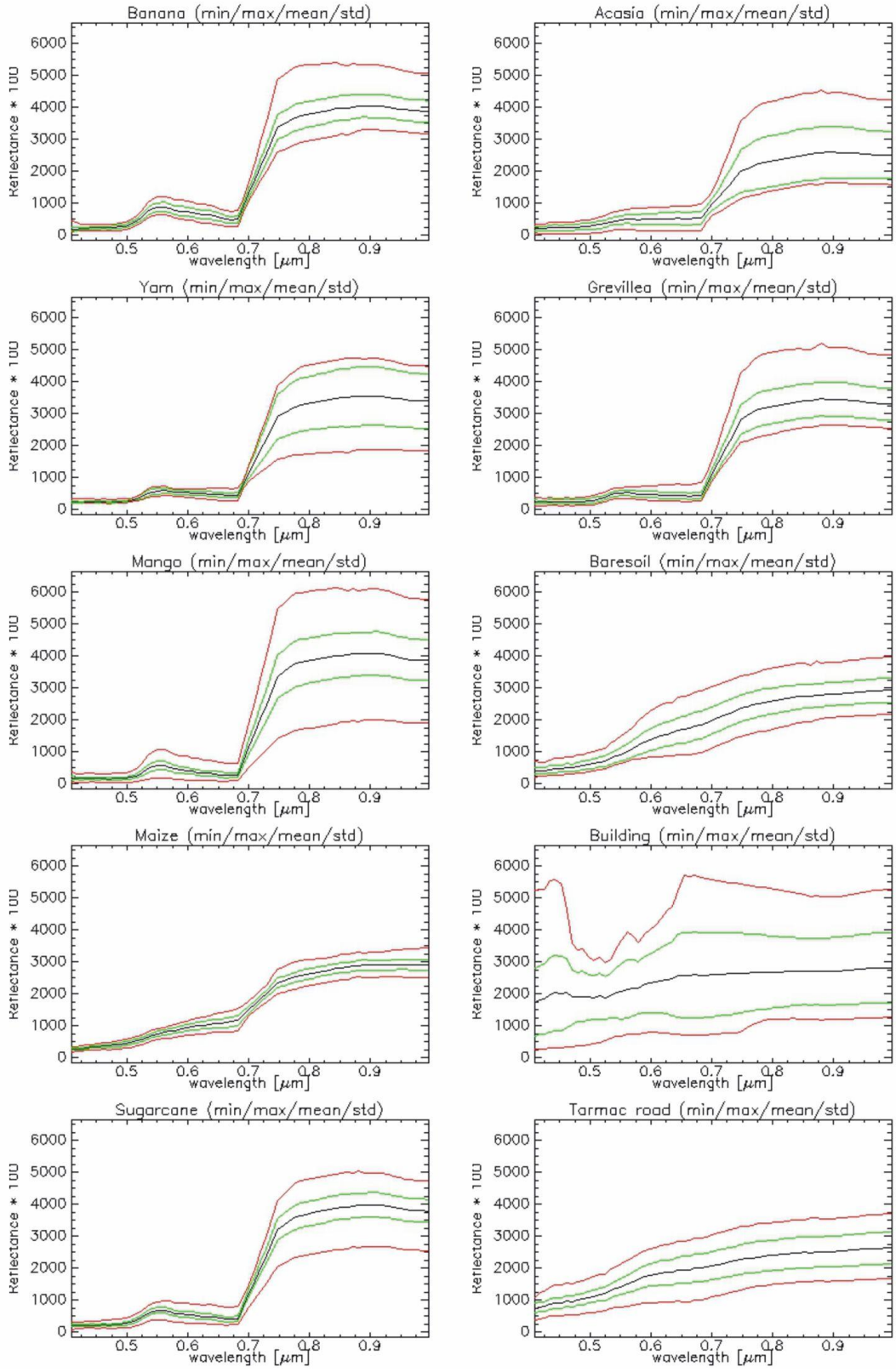

Figure 26. Spectral characteristics of known targets based on training samples (table 4) (grey = mean, green = std, red = min/max).

6.2 MNF transformed AisaEAGLE data

RGB (red-green-blue) image of first three MNF bands shows targets that are visually well separable (Figure 27). The bands do not have band covariance band to band correlations (Table 5; Table 6). Spectral variance is packed in the first bands (appendix 6). Last bands have very little variance and consist mostly of noise.

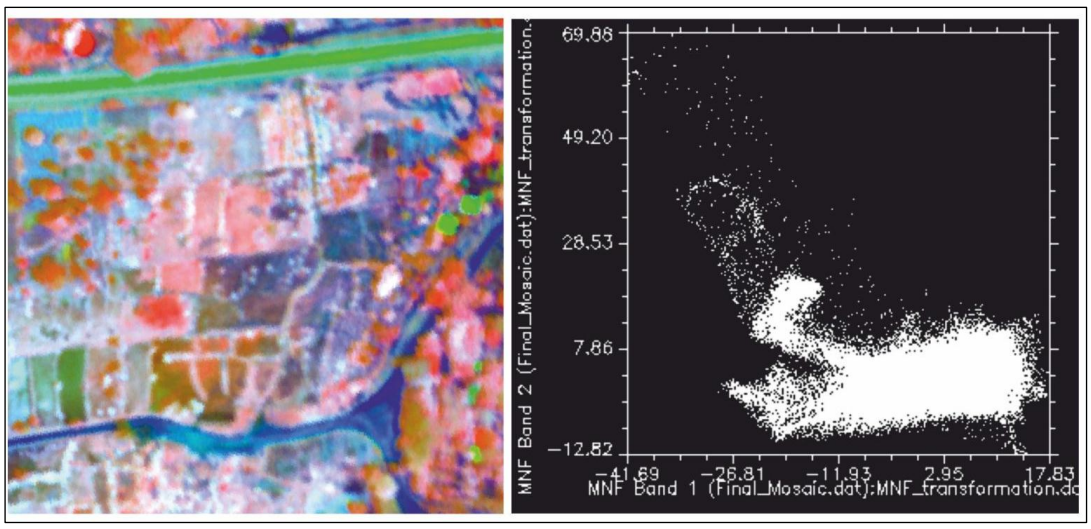

Figure 27. RGB image of first three MNF bands (left) and scatterplot of the pixel values on bands 1 and 2 for the same image area (right).

Table 5. Covariance matrix for the first 10 bands of MNF transformed AisaEAGLE data.

	Band 1	Band 2	Band 3	Band 4	Band 5	Band 6	Band 7	Band 8	Band 9	Band 10
Band 1	62.6	0	0	0	0	0	0	0	0	0
Band 2	0	36.3	0	0	0	0	0	0	0	0
Band 3	0	0	28.3	0	0	0	0	0	0	0
Band 4	0	0	0	25.7	0	0	0	0	0	0
Band 5	0	0	0	0	24.2	0	0	0	0	0
Band 6	0	0	0	0	0	15.2	0	0	0	0
Band 7	0	0	0	0	0	0	11.4	0	0	0
Band 8	0	0	0	0	0	0	0	9.2	0	0
Band 9	0	0	0	0	0	0	0	0	8	0
Band 10	0	0	0	0	0	0	0	0	0	5.7

Table 6. Band correlation matrix for the first 10 bands of MNF transformed AisaEAGLE data

	Band 1	Band 2	Band 3	Band 4	Band 5	Band 6	Band 7	Band 8	Band 9	Band 10
Band 1	1	0	0	0	0	0	0	0	0	0
Band 2	0	1	0	0	0	0	0	0	0	0
Band 3	0	0	1	0	0	0	0	0	0	0
Band 4	0	0	0	1	0	0	0	0	0	0
Band 5	0	0	0	0	1	0	0	0	0	0
Band 6	0	0	0	0	0	1	0	0	0	0
Band 7	0	0	0	0	0	0	1	0	0	0
Band 8	0	0	0	0	0	0	0	1	0	0
Band 9	0	0	0	0	0	0	0	0	1	0
Band 10	0	0	0	0	0	0	0	0	0	1

6.3 Optimum MNF bands for SVM classification

The eigenvalues for MNF transformed image range from 62.61 for band 1 to 1.22 for band 64 (Figure 28; appendix 3). The break in the curve in the Figure 28 occurs around band 12 (eigenvalue 3.63). The curve then ascends slowly until band 22 (eigenvalue 1.62). The curve for bands 23–64 is almost flat and close to 1.

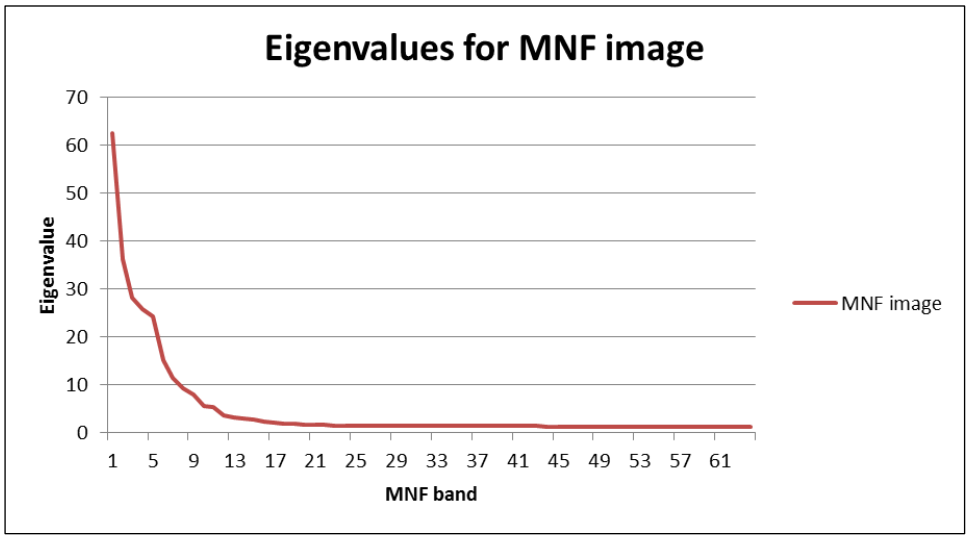

Figure 28. Eigenvalues for the AisaEAGLE data bands after MNF transformation.

The Local Moran's I index shows that there is a break in the curve around MNF band 22 (Figure 29) indicating a decrease in the clustering of similar pixel values. This indicates increasing noise. After this the slope descends slowly towards 0.

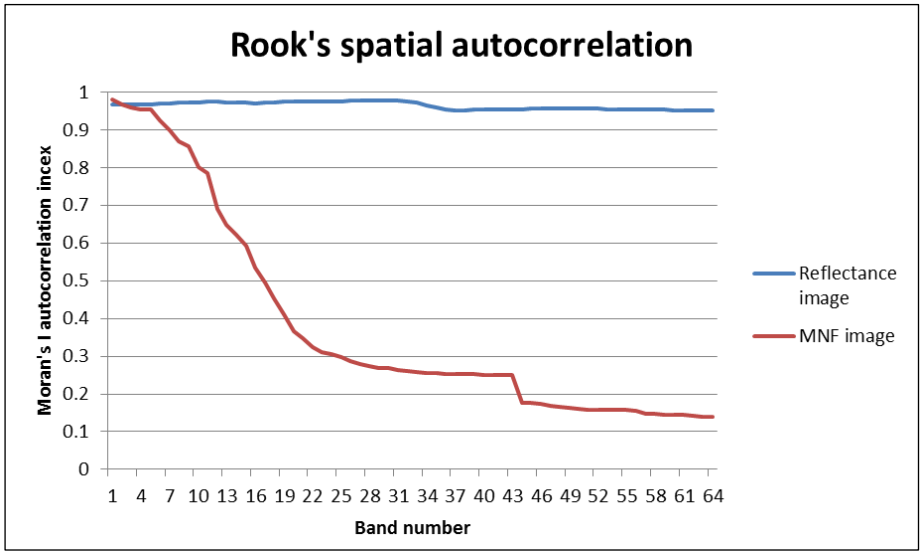

Figure 29. Moran's I (Rooks's case) autocorrelation index for reflectance image and MNF transformed image.

MNF bands 15–22 are seen as grey scale images in Figure 30. Bands 15–17 have visual resemblance to the true color reflectance image. Bands 18–20 still have some signs of buildings and trees. Bands 21 and 22 are almost completely noise and the dominant feature is the brightness difference caused by two adjacent flight lines running vertically through the images.

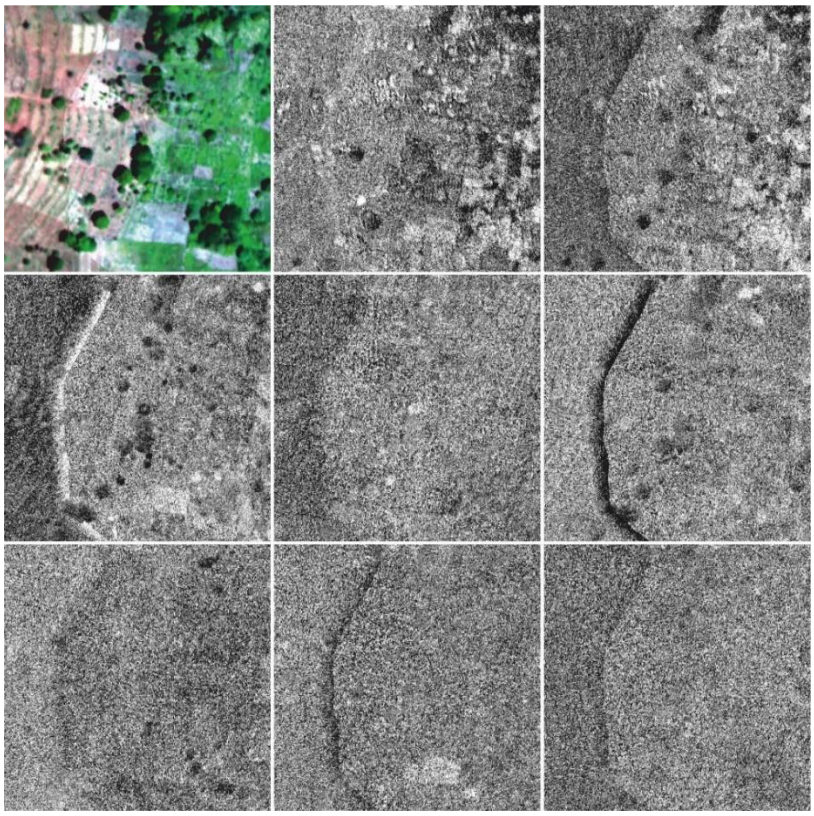

Figure 30. True color image (top left). Greyscale (linear 2% stretch) images of MNF band 15 (top center), band 16 (top right), band 17 (middle left), band 18 (middle center), band 19 (middle right), band 20 (bottom left), band 21 (bottom center) and band 22 (bottom right).

The mean MNF spectra for known targets of MNF bands 1–20 is seen in Figure 31 and Figure 32. Each agricultural crop has own distinct curves that are separable from other. The values for bands 13–20 have low variance, but the lines are still crossing each other indicating separable features.

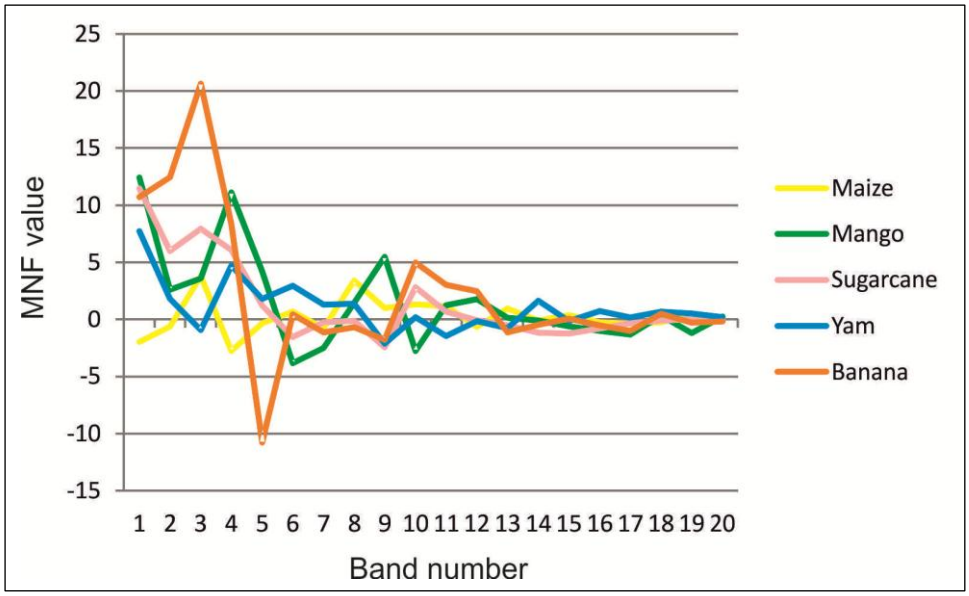

Figure 31. MNF mean for the first 20 bands of known agricultural crop targets based on training samples (table 4).

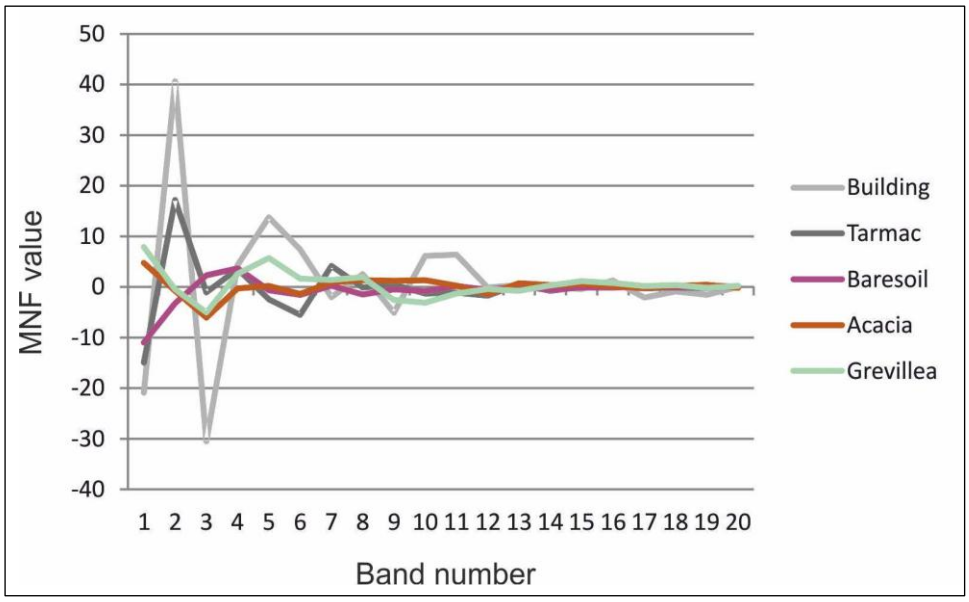

Figure 32. MNF mean for the first 20 bands of other targets based on training samples (table 4).

6.4 Results of the parameter testing of SVM classifier

All the tested gamma values gave exactly the same result as seen in Figure 33.

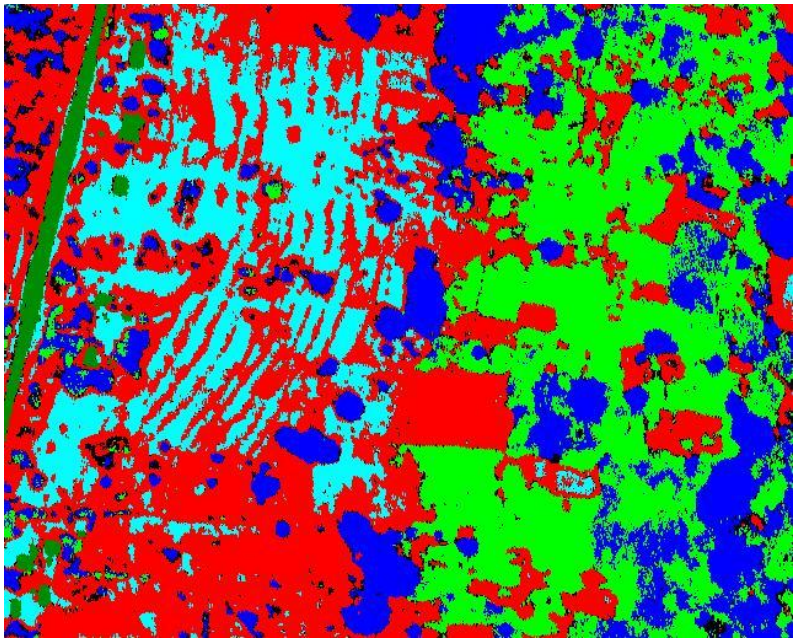

Figure 33. The classification result for plot 15 with gamma values 0.01, 0.05, 0.10, 0.50 and 100 was exactly the same. Penalty parameter was set to 100 and probability threshold to 0.50. Green = sugarcane, red = maize, blue = mango, light blue = bare soil, dark green = artificial.

ENVI change detection showed that when penalty value was increased from 50 to 100 the area of sugarcane decreased by 881 m^2 (Table 7). Maize class increased by 488 m^2 and artificial class decreased by 17 m^2.

Table 7. The change in the area of test classes measured in square meters (m^2). Penalty value for initial stage image (columns) was 50 and final state image (rows) 100.

	Unclassified	Maize	Sugarcane	Mango	Artificial	Bareground	Class Total
Unclassified	4596	179	986	246	28	112	6147
Maize	768	42329	18	0	0	391	43506
Sugarcane	187	0	28570	230	0	0	28987
Mango	309	0	294	18696	0	0	19300
Artificial	9	1	0	0	2256	1	2268
Bareground	156	508	0	0	0	18387	19051
Class Total	6025	43017	29868	19171	2285	18891	0
Class Changes	1429	688	1298	476	28	504	0
Image Difference	122	489	-881	128	-17	159	0

Visual evaluation of the classifications with penalty values 50 and 500 do not show significant differences (Figure 34). ENVI change detection (Figure 34; Table 8) shows that when penalty value was increased from 50 to 500 the area of sugarcane class decreased by 1865 m^2. The area of all other classes including the unclassified pixels increased.

Table 8. The change in the area of test classes measured in square meters (m^2). Penalty value for initial state image (columns) was 50 and final state image (rows) 500.

	Unclassified	Maize	Sugarcane	Mango	Artificial	Bareground	Class Total
Unclassified	4266	269	1373	266	18	224	6417
Maize	905	41332	18	0	4	1003	43262
Sugarcane	180	0	27472	351	0	0	28003
Mango	514	0	1004	18554	0	0	20073
Artificial	28	1	0	0	2259	18	2307
Bareground	130	1416	0	0	3	17647	19196
Class Total	6025	43017	29868	19171	2285	18891	0
Class Changes	1759	1686	2396	617	25	1245	0
Image Difference	392	244	-1865	902	23	304	0

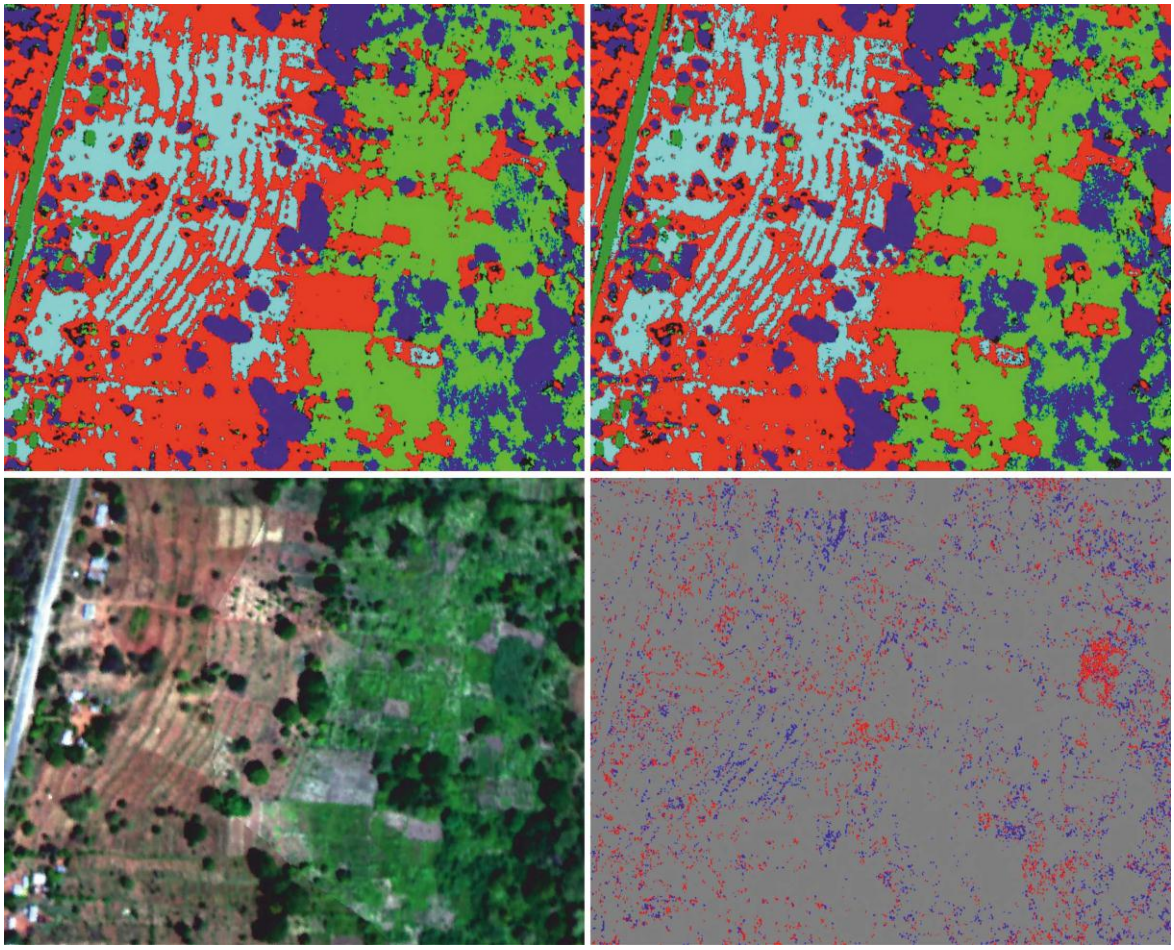

Figure 34. Classification maps with penalty value 50 (top left) and 500 (top right), true color image (bottom left), change detection (bottom right). In classification maps light blue = bare soil, blue = mango, light green = sugarcane, dark green = artificial, red = maize and black = unclassified. In change detection map red and blue both indicate a change in the assigned class.

The results of the tested probability threshold values are seen in Figure 35. Highest OA of 98.34% was achieved with probability threshold values 0.00 and 0.50 (Table 9). For threshold values 0.75–0.90 OA ascended slowly from 96.82 to 91.84%. OA for threshold value 0.95 was 84.71% and for 0.99 it dropped down to 36.31. OA_{cp} was the same as OA for threshold values 0.00 and 0.50. OA_{cp} increased to 98.96% for threshold value 0.75 and reached 100% for threshold value 0.99.

Table 9. Overall accuracy (OA), overall accuracy for classified pixels (OAcp) and the percentage of unclassified pixels for tested probability threshold values 0.00–0.99.

	OA %	OA_cp %	Unclassified %
0.00	98.34	98.34	0.00
0.50	98.34	98.34	5.15
0.75	96.82	98.96	28.29
0.80	95.92	99.34	34.03
0.85	94.65	99.60	41.04
0.90	91.84	99.59	50.34
0.95	84.71	99.70	65.57
0.99	36.31	100.00	94.42

The classified images show that when the threshold value was 0.00 all of the pixels were classified to one of the classes (Figure 35). Green square that indicates an unknown tree species and mixed grasses is classified as mango and maize pixels. Yellow circle that indicates an unknown tree species is classified as sugarcane. A known sugarcane field marked with yellow rectangle was classified correctly as sugarcane. As the probability threshold value was increased the amount of unclassified pixels increased for unknown trees and mixed grasses. When threshold value was 0.90 these targets were left completely unclassified. As the threshold value was increased the amount of unclassified pixels for the known sugarcane field increased correspondingly but less significantly. At threshold value 0.90 most of the field was still classified correctly. At value 0.99 over half of the field is left unclassified.

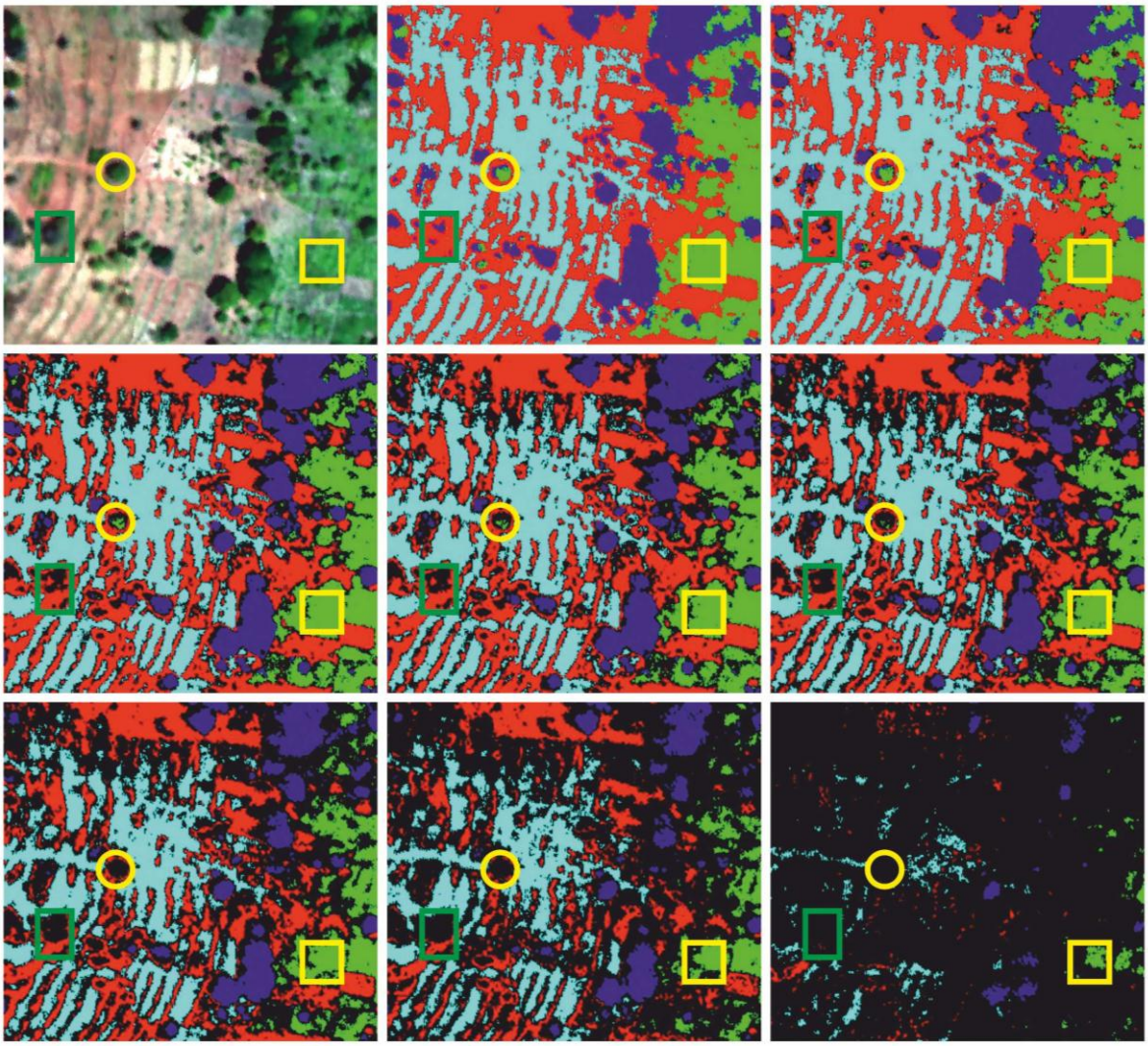

Figure 35. True color image (top left), classification result for plot 15 with probability threshold 0 (top center), 0.50 (top right), 0.75 (middle left), 0.80 (middle center), 0.85 (middle right), 0.90 (bottom left), 0.95 (bottom center), 0.99 (bottom right). Classification colors: red = maize, light green = sugarcane, blue = mango, light blue = bare soil, black = unclassified. Green square indicates an unknown tree and mixed grasses, yellow circle indicates an unknown tree and yello square a known sugarcane field.

6.5 The impact of MNF transformation on the classification accuracy

OA of the reflectance based classification was 80.68% (Table 10). OA of the MNF based classification was 91.52% (Table 11). PA was the same for maize in both classifications. PA for all other agricultural targets increased when MNF transformation was used. UA increased for all other agricultural classes except for banana. PA for yam increased from 1.9 to 66.4% after the transformation and UA from 14.3 to 77.5%.

Table 10. Classification accuracy statistics for reflectance based classification. OA was 80.58% and kappa 0.78.

	PA %	UA %	EC %	EO %
Building	89.8	99.5	0.5	10.2
Maize	91.7	88.0	12.0	8.3
Mango	79.5	77.4	22.6	20.5
Tarmac	97.8	88.0	12.0	2.2
Sugarcane	88.2	65.2	34.8	11.8
Yam	1.9	14.3	85.7	98.1
Baresoil	96.4	96.4	3.6	3.6
Acacia	64.3	50.6	49.4	35.7
Grevillea	47.1	66.7	33.3	52.9
Banana	85.7	89.6	10.5	14.3

Table 11. Classification accuracy statistics for MNF (20 band) based classification. OA was 91.52% and kappa 0.90.

	PA %	UA %	EC %	EO %
Building	97.1	98.5	1.5	2.9
Maize	91.7	94.3	5.7	8.3
Mango	90.3	98.8	1.2	9.7
Tarmac	97.2	96.7	3.3	2.8
Sugarcane	90.8	88.5	11.5	9.2
Yam	66.4	77.5	22.5	33.7
Baresoil	99.0	96.5	3.5	1.0
Acasia	84.3	72.0	28.1	15.7
Grevillea	78.4	76.9	23.1	21.6
Banana	95.7	88.7	11.3	4.3

6.6 Results of the crop classifications of the study area

The results of the crop classifications of the full study area are seen in Figure 36.

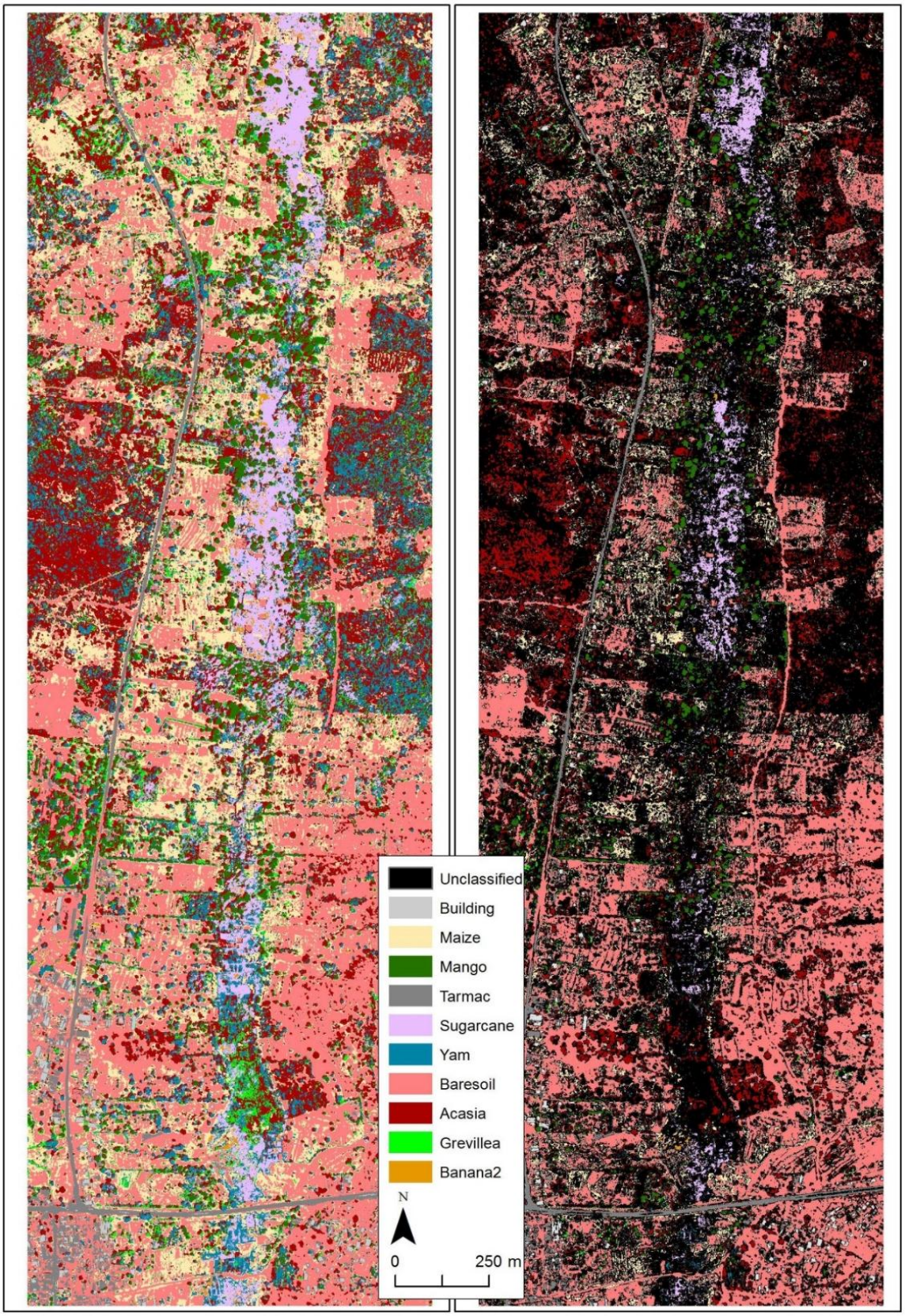

Figure 36. Classification of the study area with probability threshold values 0.00 (left) and 0.90 (right).

OA and OA_{cp} for the classification done with probability threshold value 0.00 was 91.52% (Table 12). OA for classification done with probability threshold 0.90 was 68.24% and OA_{cp} 99.70% (Table 13) while 61.02% of pixels were left unclassified (Table 14). When probability threshold was 0.00 PA for individual classes ranged from 66.4 to 99.0%. PA values for all classes decreased as the probability threshold was increased to 0.90. PA for yam dropped to 2.88%. UA values on the contrary increased for all the classes. 7 out of 10 classes have 100% UA when probability threshold is 0.90. The full confusion matrices for the classifications are seen in Table 15 and Table 16.

Table 12. Classification accuracy statistics for classification done with probability threshold 0.00. OA of the classification was 91.52%, OAcp 91.52% and kappa 0.90.

	PA%	UA%	EC%	EO%
Building	97.1	98.5	1.5	2.9
Maize	91.7	94.3	5.7	8.3
Mango	90.3	98.8	1.2	9.7
Tarmac	97.2	96.7	3.3	2.8
Sugarcane	90.8	88.5	11.5	9.2
Yam	66.4	77.5	22.5	33.7
Baresoil	99.0	96.5	3.5	1.0
Acacia	84.3	72.0	28.1	15.7
Grevillea	78.4	76.9	23.1	21.6
Banana	95.7	88.7	11.3	4.3

Table 13. Classification accuracy statistics for classification done with probability threshold 0.90. OA of the classification 68.24%, OAcp 99.70% and kappa 0.65.

	PA%	UA%	EC%	EO%
Building	87.3	100.0	0.0	12.7
Maize	66.7	100.0	0.0	33.3
Mango	78.9	100.0	0.0	21.1
Tarmac	91.7	99.4	0.6	8.3
Sugarcane	65.6	99.4	0.6	34.5
Yam	2.9	100.0	0.0	97.1
Baresoil	79.4	100.0	0.0	20.6
Acacia	41.4	96.7	3.3	58.6
Grevilela	41.2	100.0	0.0	58.8
Banana	57.9	100.0	0.0	42.1

Table 14. Number and percentage of classified pixels per class for Figure 36.

	prob 0.00 (Npts)	prob. 0.00 (%)	prob. 0.90 (Npts)	prob. 0.90 (%)
Unclassified	0	0.00	6318832	61.02
Building	85837	0.83	63626	0.61
Maize	2044942	19.75	687790	6.64
Mango	474570	4.58	175859	1.70
Tarmac	267995	2.59	180743	1.75
Sugarcane	650525	6.28	172427	1.67
Yam	1054354	10.18	20068	0.19
Baresoil	2908781	28.09	2011890	19.43
Acacia	2351519	22.71	670814	6.48
Grevillea	449942	4.35	45291	0.44
Banana	66935	0.65	8060	0.08

Table 15. Confusion matrix of testing samples (columns) and the classes they were assigned to (rows) with probability threshold 0.00.

	Building	Maize	Mango	Tarmac	Sugarc.	Yam	Bares.	Acacia	Grevil.	Banana	Class t.
Unclassified	0	0	0	0	0	0	0	0	0	0	0
Building	199	0	0	3	0	0	0	0	0	0	202
Maize	0	66	0	1	0	0	2	1	0	0	70
Mango	0	0	167	0	2	0	0	0	0	0	169
Tarmac roac	6	0	0	175	0	0	0	0	0	0	181
Sugarcane	0	0	1	0	216	17	0	4	0	6	244
Yam	0	0	0	0	7	69	0	5	8	0	89
Baresoil	0	6	0	1	0	0	192	0	0	0	199
Acacia	0	0	11	0	0	9	0	59	3	0	82
Grevillea	0	0	2	0	0	9	0	1	40	0	52
Banana	0	0	4	0	13	0	0	0	0	134	151
Testing total	205	72	185	180	238	104	194	70	51	140	1439

Table 16. Confusion matrix of testing samples (columns) and the classes they were assigned to (rows) with probability threshold 0.90.

	Building	Maize	Mango	Tarmac	Sugarc.	Yam	Bares.	Acacia	Grevil.	Banana	Total
Unclassified	25	24	38	15	82	100	40	41	30	59	454
Building	179	0	0	0	0	0	0	0	0	0	179
Maize	0	48	0	0	0	0	0	0	0	0	48
Mango	0	0	146	0	0	0	0	0	0	0	146
Tarmac roac	1	0	0	165	0	0	0	0	0	0	166
Sugarcane	0	0	1	0	156	0	0	0	0	0	157
Yam	0	0	0	0	0	3	0	0	0	0	3
Baresoil	0	0	0	0	0	0	154	0	0	0	154
Acacia	0	0	0	0	0	1	0	29	0	0	30
Grevillea	0	0	0	0	0	0	0	0	21	0	21
Banana	0	0	0	0	0	0	0	0	0	81	81
Total	205	72	185	180	238	104	194	70	51	140	1439

7. DISCUSSION

7.1 Assessment of the geometric accuracy AisaEAGLE data

The geometric accuracy of the AisaEAGLE data was sufficient for the mapping of the distribution of the agricultural crops in the study area. The small distortions on the edges of the flight lines did not have significant effect on the data when it was seen from the scale of the full study area. These distortions will however have minor impact on the measured area of the target species. The geometric accuracy could be improved by using a higher accuracy DEM. Another possible source of error was the boresight parameters that were used. Although the AisaEAGLE sensor and the Oxford RT3100 GPS/INS units were not detached between the two flight campaigns in Hyytiälä and the Taita Hills it is possible that the units have moved slightly in relation to each other during the transportation of the imaging system to Kenya or the installation of the equipment to the aircraft. Third source of error was the sensor model file that was used in Parge. After this dataset was processed a new calibration file has been received from Specim (2014) where a more precise method has been used to determine the position of each pixel from the optical center of the sensor.

7.2 Assessment and interpretation of the atmospherically corrected AisaEAGLE data

ATCOR-4 corrected the small peak around 450 nm that was caused by atmospheric scattering (Figure 21). The absorption valleys of atmospheric water vapor were also successfully corrected in the 800 and 950 nm regions (Figure 21). Low reflectance values around 450 nm for all vegetation targets (Figure 26) can be explained by the absorption maximums of chlorophylls and carotenoids in this region (Ustin et al. 2009). The reflectance values increased in the 550 nm region. This was caused by the relatively lower chlorophyll absorption in this region (Clevers et al. 2002). For maize the increase of reflectance values towards 550 nm started earlier than for other targets. Banana, yam, mango and maize have absorption valleys around 650 nm where chlorophylls have second absorption maximum. Reflectance of maize increased evenly towards the NIR region and shared similarities with bare soil reflectance. This indicates that the photosynthetic activity was very low or had completely stopped. This was supported by field observations of very dry maize found in the area (Figure 37). Maize plants are sparsely planted and they generally cover only small area of land. This increases the soil impact on the reflectance curve that may explain part of the resemblance to bare soil. Red edge for vegetation targets started around 680 nm and evened out around 750 nm as expected (Baranoski & Rokne

2005). The high reflectance values between 750 and 900 nm are caused by the spongy mesophyll cells and the effect of leaf additive reflectance (Gates et al. 1965; Jensen 2000). Reflectance of vegetation targets decreased after 900 nm. This was caused by plant water absorption (Peñuelas et al. 1993). This feature was not present for maize. It also shows that ATCOR-4 has successfully corrected the atmospheric water vapor absorption seen in Figure 21 without removing the plant water absorption feature.

Figure 37. Photograph of very dry maize found in the study area. Photograph taken by Rami Piiroinen in February of 2012 in the study area.

7.3 Selecting optimum MNF bands for the classification based on test results

The test results showed that after MNF transformation most of the spectral information was packed in the first bands as was expected (Figure 28; Figure 29) and that the noise increased with the band number (appendix 6; Figure 30; Green et al. 1988; RSI 2004). There was a break in the eigenvalue plot (Figure 28) around band 12. The curve ascended slowly until band 22. After this the curve was almost flat and values were close to 1. The break in the curve of the Moran's I spatial autocorrelation index (Figure 29) was around band 22. As Moran's I index indicates clustering of similar values it was concluded that until band 22 there were some recognizable shapes left. Based on these notions the bands 15–22 were chosen for closer visual analysis (Figure 30). The last band that showed some resemblance to the true color image was band 20. After this the images were dominated by noise. Based on this analysis it was concluded that only MNF bands 1–20 should be used

in the classification. In a similar study by Ghosh et al. (2014) 25 MNF bands derived from VNIR/SWIR spectral region HyMap data were used for the classification. Zhang & Xie (2012) used 15 MNF bands in their study derived from 224 band AVIRIS data.

7.4 Selecting optimum parameters for classification based on test results

The test results showed that gamma value did not have impact on the classification result in this case (Figure 33). Thus the default value given by ENVI was used for the classification as was done in previous study by Petropoulos et al. (2009). Different penalty values showed minor changes in the classification result (Figure 34, Table 8, Table 7). When the penalty value was increased from 50 to 100 the sugarcane class lost 881 m^2 of its area. Artificial class decreased by 17 m^2. The decrease of these areas was seen as increase in all other classes. When the penalty value was increased from 50 to 500 the changes in the area of classes followed the same trend except for artificial class, which increased by 23 m^2. The area of sugarcane class decreased now by 1895 m^2. This means 6.24% decrease in the area of sugarcane class. The area of unclassified pixels increased by 392 m^2. This means that when the penalty value was increased more pixels were left unclassified. This indicates that higher penalty values did create a more accurate model that allowed fewer misclassifications (ENVI help 2014; Cortes & Vapnik 1995). Overall the impact of the penalty parameter on the classification result was not very significant as the changes were small when compared to the class totals (Table 8; Table 7). Due to these reasons the ENVI default value of 100.0 was considered to be a valid option. This decision was supported by a similar study by Petropoulos et al. (2012) where default gamma and penalty values were used with RBF kernel.

The test results for probability threshold values (Table 9) showed that the OA was highest when the threshold value was 0.00. OA_{cp} was the same as OA with threshold 0.00, since all pixels were classified into one of the classes. It is known that the 5 classes used in the testing do not cover the whole study area (Figure 12). For this reason it was meaningful to test higher probability threshold values. The results showed that as the threshold value was increased the OA decreased. The reason for this was that more testing samples were left unclassified (appendix 4; appendix 5). However OA_{cp} increased which means that the pixels that were classified were being classified with higher accuracy. With probability threshold 0.99 a pixel will be classified only if it has over 99% probability to belong to one of the classes. Thus 94.42% of the pixels were unclassified. The remaining pixels were

classified with 100% accuracy, which means that none of the pixels were misclassified to wrong class. Considering this the OA of 36.31% was still relatively high for threshold 0.99.

The impact of probability threshold value was further analyzed from classified images with different threshold values (Figure 35). The results showed that with threshold value 0.00 the unknown trees and grasses were falsely classified as mango and sugarcane. The known sugarcane field was correctly classified. An optimal threshold value would leave the unknown targets unclassified while the known sugarcane field would be correctly classified. This level was reached at threshold value 0.90 as the unknown targets were completely unclassified and most of the sugarcane field was still correctly classified. Higher values only increased the number of unclassified pixels for the known sugarcane field.

Based on this analysis the optimal threshold value in this case was determined to be 0.90. At this level the OA was 91.84%, OA_{cp} 99.59% and 50% of the pixels were classified to one of the classes. In previous studies by Ghosh et al. (2014) and Petropoulos et al. (2012) threshold value 0.00 was used. However the optimal threshold value depends on how heterogeneous the target area is and how specific the classes are. Thus the classification of the full study area was done with probability threshold 0.90. Another classification with threshold 0.00 was done for referencing purposes.

7.5 Analysis of the crop classification results

The results of the crop classifications of the full study area are seen in Figure 36. Overall accuracy with probability threshold value 0.00 was 91.52% (Table 12) and all of the pixels were classified (Figure 36). It is known that this cannot be true since there were over 50 plant species mapped from the study plots (appendix 1; Figure 12). The overall accuracy of the classified pixels (OA_{cp}) for the classification done with 0.90 threshold was 99.70% while 61% of the pixels were unclassified (Table 14). With threshold 0.90 UA was 100% for 7 of the classes, which means that the classes did not get mixed with each other (Table 13). PA however decreased for all of the classes when compared to classification with threshold 0.00 (Table 12). The reason for lower PA is that less testing samples were correctly classified. UA increased as fewer pixels were misclassified to other classes (Table 15; Table 16). Higher probability threshold value removed almost totally the misclassifications between classes as seen in Table 15 and Table 16. However it also

decreased the total number of correctly classified pixels. Thus in the classified image with threshold value 0.90 the pixels are more likely to represent the same class on the ground while the unclassified areas contain pixels from the target classes. In the classification with threshold 0.00 more testing samples were classified correctly, but there was more misclassifications between classes and the classes contained more pixels that did not belong to any of the classes. Based on these notions it can be argued that if these classifications are used for the study of the spatial distributions of these species the classification done with threshold 0.90 should be used as there are more certainty that the pixels are correctly classified and large amount of pixels that did not belong to any of the classes were left unclassified. In the study by Ghosh et al. (2014) probability threshold value 0.00 was used. In their study this was a valid choice since most of their study area was covered with known tree species and non-forest targets were masked out from the classification. In a study by Petropoulos et al. (2012) threshold value 0.00 was used while the classes included targets such as permanent crops, natural grasslands and heterogeneous agricultural areas. In their study threshold value 0.00 was a valid choice since the classes were on higher hierarchical level.

The spatial resolution in the studies by Ghosh et al. (2014) and Petropoulos et al. (2012) ranged from 4 to 30 meters. In this thesis the pixel size was 0.6 meters. High spatial resolution was useful for the identification of maize plants that covered only one or few pixels. A single mango tree however consisted of dozens of pixels (Figure 38). When the probability threshold value was 0.00 the mango tree was classified correctly on the sunny side. On the shadowed side some of the pixels were misclassified as yam and acacia. With probability threshold value 0.90 these misclassifications were left unclassified. This observation further proves the advantages of the higher probability threshold level in this case.

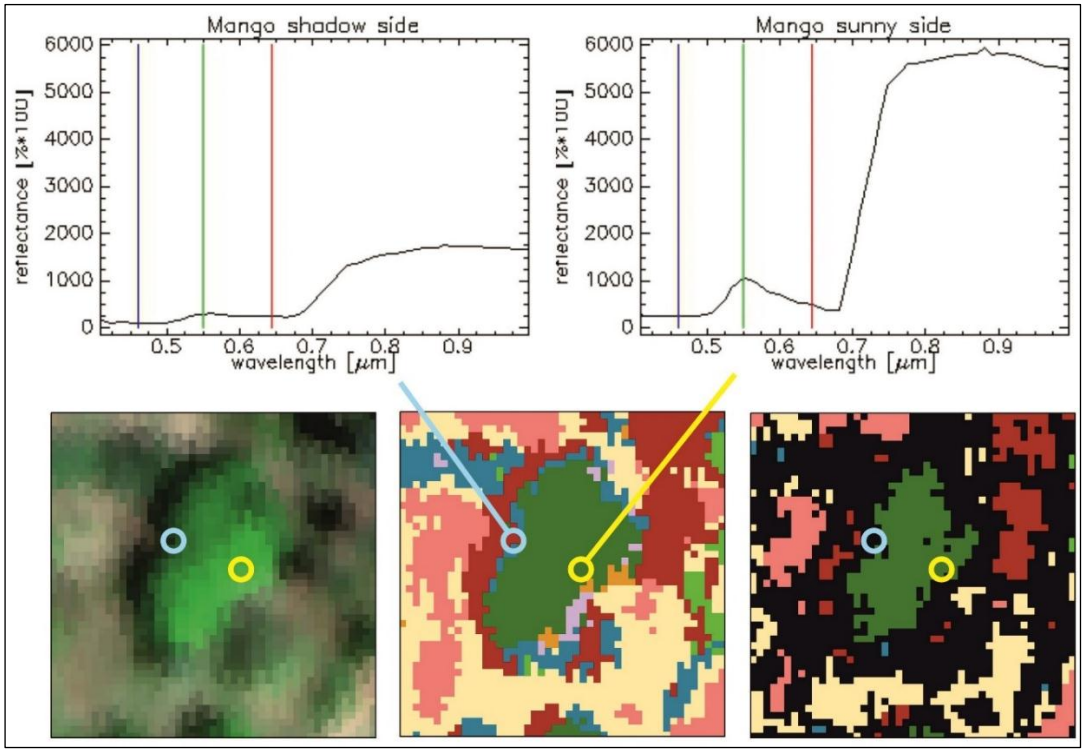

Figure 38. True color image of a known mango tree (bottom left), classifications with probability threshold values 0.00 (bottom middle) and 0.90 (bottom right). Blue circle indicates the reflectance from the shadow side of the tree and yellow the reflectance from the sunny side. In classified images dark green = mango, dark red = acacia, blue = yam and black = unclassified.

There were plenty of yam targets at the middle of the classified image done with threshold 0.00 on both sides of the valley (Figure 36).These are likely to be misclassifications as yams was only found in small quantities in the moist areas of the valley during the ground survey (appendix 1; Figure 12). In the classification with threshold value 0.90 these areas were left unclassified. However the amount of correctly classified yam targets decreased from 69 to only 3. This means that the higher threshold removed the large misclassified areas of yam but it also decreased the correctly classified yam targets significantly. This decrease was however much stronger for yam than for any other classes, which indicates that there might have been something wrong with the field mapping or training samples of yam targets.

The classification done with 0.90 threshold show that sugarcane was found exclusively in the valley bottom. Maize fields were clustered near the two major roads. Banana plants were found as single plants or small clusters near other agricultural crops and buildings. Mango trees were located on both sides of the river. Further away from the river valley where bare soil was dominant feature the most common tree was acacia and only few mango trees were found. Yam was found in small scale from the valley bottom. For both

classifications the most common agricultural crop was maize. This was supported by the observations in the field. In the classification with threshold value 0.00 the second most common agricultural crop was yam whereas in the classification with threshold 0.90 yams was the least common agricultural crop.

7.6 Evaluation of the classification methodology

Hughes phenomenon (Hughes 1968; Alonso et al. 2011) was successfully dealt with MNF transformation. Noise and the dimensionality of the data was reduced as the transformation packed the spectral information on first bands and the bands 21–64 were left out of the classification. MNF transformation increased the overall accuracy of the classification from 80.58% to 91.52% when it was compared to the classification that was done on data in reflectance values (Table 10; Table 11). This was expected based on the study results by Ghosh et al. (2014). The results of this thesis showed that this method was capable of separating the studied plant species with very high accuracies. However the heterogeneous nature of the study area and the abundance of plant species made it difficult to find a way to classify only the target species while leaving other targets unclassified. This problem was approached by adjusting the probability threshold value. The possibility to do so is a great advantage of SVM classifier and makes it suitable for various purposes. Gamma value did not have any effect on the classification result which was highly unexpected. This was unexpected since the gamma value controls the transformation of the input data into higher dimensional feature space (Pal & Watanachaturaporn 2004; Canty 2010). This should have impact on how the separating hyperplanes are defined and thus how the classes are formed and how pixels are classified. In studies by Kuemmerle et al. (2009) and Petropoulos et al. (2012) different combinations of gamma values were tested but neither of the studies shares the results of these tests. There was no previous study available that could have helped to explain this and the reason remains unknown. Penalty parameter had only minor impact on the results based on the parameter testing. However the testing was done with only three values and higher values might have had bigger impact. It is also possible that this parameter would have more impact on the results when the classification was applied on the full study area.

There are other methods that are also showing great promise in species identification from hyperspectral data. Especially interesting is the spectranomics method described by Asner & Martin (2009) where the classification is based on plant pigment, plant water, nitrogen

and phosphorus content that are first measured from hyperspectral data. The advantage of the spectranomics method is that theoretically it is possible to gather extensive library of the chemical and structural composition of plant species and theoretically the measurements made in different geographic locations could be classified without ground reference information. The method used in this thesis is highly depended on the specific geographical area. When MNF transformation is applied before the classification all the values become strongly scene specific as the resulting MNF bands are formed as compositions of all the spectral characteristics found in the study area. Thus it is not possible to create spectral library from MNF transformed data that could be applied in other geographic areas.

Classifications in this thesis were based on individual pixels. Other studies have shown that the classification results could be improved by applying the classification on objects that are derived from the data before classification (Li et al. 2007; Weih & Riggan 2010). In object-based classification the pixels are aggregated into spectrally homogenous objects using image segmentation algorithms. The classification is then applied on the objects. This reduces the within-class spectral variation and generally removes the salt-and-pepper effects typical with high spatial accuracy classifications (Weih & Riggan 2010; Liu & Xia 2010). Salt-and-pepper effect refers to a situation where adjacent pixels from the same target are assigned to different classes (Yu et al. 2006). This effect was very strong in the preliminary tests done with 42 vegetation classes. The effect was still visible in the classification done with probability threshold value 0.00 (Figure 36; Figure 38) as tree targets were in some cases assigned to different classes on sunny and shadowed sides with heavy mixing of adjacent pixels (Figure 38). Increasing the probability threshold value lessened this effect, but it could be further handled with object-based approach. The segmentation could also be done with LiDAR (light detection and ranging) data that would give three dimensional structure for each object (Asner et al. 2009). Then classification can be applied only on the brightest pixels of each object and the structural information can be used to improve the accuracy (Asner et al. 2009; Benz et al. 2004).

7.7 The results in the context of CHIESA project

The results of this thesis showed that the used classification method was able to identify agricultural crops from the AisaEAGLE data acquired for the campaign. MNF transformation did improve the classification result and SVM classifier yielded good

results. For future use of this method it is important to note that the training samples should be collected only from classes that have enough observations to get hundreds of training samples. The classification should be limited to reasonable amount of classes. The first attempts with 50 classes where only few samples were found for some of the classes were not successful. The samples need to be collected from target points that are expected to give a good signal. For example the samples should not be collected from the shadowed sides of the trees. These areas will then be left unclassified when the threshold values is increased to the optimum level. The optimum threshold value needs to be searched manually with the method used in this thesis. Also the correct subset of MNF bands needs to be searched manually with the method described in this thesis. Based on the test results the standard gamma and penalty values given by ENVI were valid choices and can be used in future classifications. However further research on the effect of penalty value on the classification results would be worthwhile.

The focus in this thesis was the classification methodology. After the proposed improvements presented in previous chapter this method is now ready to be used for the classification of the whole CHIESA study transect. This larger scale study of the distribution of the agricultural crops could reveal valuable information of the ecosystem functioning in the Taita Hills. The distribution of agricultural crops could be further studied together with other variables such as water resources and fauna to reveal the full ecosystem functioning.

7.8 Assessment of the field campaign and the data processing procedure

The flight campaign was mainly successful and the data does not have major issues with clouds or holes in the data caused by too narrow overlaps for flight lines. However some haze was found that can be seen as blurriness in Figure 25. The only real mistake was the use of the wrong undulation mode in the Oxford RT3100 settings. For this reason the output flight altitudes needed in geometric correction were measured from EGM96 geoid instead of WGS84 reference plane. Parge did not have option to use EGM96 elevation values so the problem was solved by using a self-defined coordinate system and adding a false elevation value to the used DEM that approximately corrected the difference between these two reference systems. Radiometric correction procedure was successful after preliminary problems. There was confusion between the FWHM values and spectral sampling values delivered by the sensor manufacturer (Figure 18). This was however

solved and the spectral sampling values were used in the processing. For future projects the use of FWHM values instead of spectral sampling values should be considered as FWHM values are physically measured whereas the sampling values are only approximations of these measurements. The FODIS-ratios were calculated and tested but did not show good results. These however were not needed in any part of the process. The missing FODIS channels caused problems in the boresight calibration and geometric correction as the programs had difficulties in handling data that had wider FOV on one side and narrower on the other. For campaigns like these the FODIS sensor is not needed and could be completely removed. After removing the FODIS sensor AisaEAGLE would have a wider FOV that allows wider gaps between flight lines and thus would save flight time.

The geometric correction of very long flight lines caused problems as the capacity of the computers were on the limits when handling files that were 20 to 30 GB large. The reason for such large files was that the ENVI BSQ and BIL file types can handle only rectangular objects that have pixel values assigned to each pixel on all bands even in the areas where there was no data. The flights were done in intermediate directions, which increased the size of the image rectangles when compared to lines flown in cardinal directions. This increased the size of individual flight lines significantly. The flight lines were not planned in cardinal directions since they followed the study transect to optimize the flight hours (Figure 10). However the flight lines between Mwatate and Wundanyi could have been planned as shorter lines in north-south direction without significant difference on the total flight kilometres. However more turns between flight lines takes additional time. The original idea was to fly the flight lines according to sun azimuth angles, which was expected to lessen the BRDF effects on the data. However this caused many problems as the flights needed to be flown at a certain time that caused problems due to practical limitations of weather and other issues related to flying. Planning the flight lines in north-south direction should be a viable option in most of the cases especially near the equator where sun rises fast to high elevations lessening the BRDF effects. Flying in east-west directions should be avoided especially further away from the equator where sun elevation is generally lower and BRDF effects higher.

During the field campaign spectroscopic measurements were made for the target plant species with the purpose of using them as training material for the classification. These measurements were not however used in this campaign as the measurements showed too much variation caused even by very small differences in the position of the handheld spectrometer over the target plants. Additionally there was no real need for these

measurements as the training samples were collected from the AisaEAGLE data based on the vegetation maps. The spectroscopic measurements would have been more useful if they had been made primarily for open road or bare soil targets. Then these measurements could have been used to validate the atmospheric correction. Few of these kinds of measurements were made but they were not located in the study area of this thesis. Also getting spectral measurements from trees or other tall plant species was very difficult in practice. However the used measurements could be used in the future for the study of the plant health as lot of notes was written of the condition of each plant target. This information could then be used to identify features from the spectral signatures that indicate the plants that are under stress or have some disease.

8. CONCLUSIONS

The main objective of this thesis was to develop a crop classification method using high spatial and spectral resolution imaging spectroscopy AisaEAGLE data. The classification method that was used yielded good overall accuracies. MNF transformation improved the classification results significantly. Method for defining the optimal number of MNF bands was introduced and applied successfully. SVM classifier used with RBF kernel yielded good results that were in good correlation with previous studies. Gamma parameter for the SVM classifier did not have any impact on the results. The reason for this remains unknown. Penalty parameter had only minor impact on the classification results in this case. Probability threshold parameter was the most significant parameter and was given further attention. A method for finding an optimal threshold value was introduced and applied. Adjusting threshold level was especially important in this case since the study area was heterogeneous and only fraction of the species that were mapped were used in the classification. For further use this classification method should be combined with object-based classification approach. This is expected to lessen the salt-and-pepper effects and improve the classification accuracy especially for tree targets that experience heavy BRDF effects. Before MNF transformation is applied the non-vegetation targets should be masked out. After these modifications are made the method can be applied in further classifications of the CHIESA study transect. A working method was developed and future improvements were suggested and thus the main objective of this thesis was successfully completed.

The second objective was to develop the process of planning and executing imaging spectroscopy data acquisition campaigns. The flight elevation data was stored in EGM96 reference system. This caused problems in geometric correction as Parge did not recognize this system. In future campaigns WGS84 reference plane should always be used. FODIS measurements were of poor quality and were not needed since atmospheric correction was applied on the data. For future use the FODIS sensor should be removed if possible. This would give the AisaEAGLE sensor wider FOV that is even on both sides from the optical center. Boresight calibration could not be applied since CaliGeo could not handle FOV that was wider on the other side from the optical center. Boresight values that were used have been calculated before for another campaign in Hyytiälä, Finland in 2011 with Parge. AisaEAGLE and GPS/IMU unit might have moved slightly during the transportation and installation of the equipment for this campaign. This would make the old boresight values invalid. This was one possible reason for the small distortions on the sides of the images. DEM that was used was very low quality. The study area of this thesis was relatively flat

and the poor quality of the DEM did not cause major issues. In the mountainous areas of the CHIESA study transect this would cause more problems and alternative sources of elevation data must be considered. Atmospheric correction was done using spectral sampling values. For future use the true FWHM values should be used, since they are physically measured in laboratory. The second objective was successfully completed as all the problems faced in the project are stored in this thesis and will be shared with all the participants of the campaign.

ACKNOWLEDGEMENTS

This thesis could not have been possible without the effort of all the people working as part of the CHIESA project. Special thanks go to Prof. Dr. Petri Pellikka, Dr. Mika Siljander, Pekka Hurskainen, Mark Boitt, Samuel Nthuni and Arto Viinikka with whom the field work was conducted. Taita Research Station of University of Helsinki provided a much needed safe haven in this remote location, which was essential for the successful field work. The staff of the station including Mwadime Mjomba, Granton Righa, Darius Kimuzi, Rebecca Mwanyolo and Elphinstonde Kalagha provided help in all the things that was needed during the stay. Special thanks go to Darius Kimuzi whose help together with other local guides with the identification of plant species was crucial for the successful field mapping. I would like to thank Prof. Dr. Petri Pellikka and Dr. Matti Mõttus for the guidance throughout the thesis. Special thanks goes to Tuure Takala for technical guidance in all things related to the processing of the AisaEAGLE data and to Janne Heiskanen for many helpful tips related to the methodology. Finally I would like to thank the Specim team: Petri Nygren, Markku Koskela, Antti-Jussi Mattila and Rainer Bärs for the technical support related to the AisaEAGLE sensor system.

REFERENCES

Aggarwal, S. (2004). Principles of remote sensing. In Sivakumar, M. V. K., P. S. Roy, K. Harmsen & S. K. Saha (eds.). *Satellite remote sensing and GIS applications in agricultural meteorology*, 23–38. World Meteorological Organisation, Geneva.

Alonso, M. C., J. A. Malpica & A. M. de Agirre (2011). Consequences of the Hughes phenomenon on some classification techniques. *ASPRS 2011 Annual Conference*. 1.5–5.5 2011, Milwaukee, Wisconsin.

Asner, G. P. & R. E. Martin (2009). Airborne spectranomics: mapping canopy chemical and taxonomic diversity in tropical forests. *Frontiers in Ecology and the Environment* 7, 269–276.

Baranoski, G. V. & J. G. Rokne (2005). A practical approach for estimating the red edge position of plant leaf reflectance. *International Journal of Remote Sensing* 26: 3, 503–521.

Bellman, R. (1961). *Adaptive control processes: a guided tour*. Princeton University Press.

Bennet, K. P. & O. L. Mangasarian (1992). Robust linear programming of two linearly inseparable sets. *Optimization Methods and Software* 1, 23–24.

Benz, U. C., T. Hoffmann, G. Willhauck, I. Lingenfelder & M. Heynen (2004). Multi-resolution, object-oriented fuzzy analysis of remote sensing data for GIS-ready information. *ISPRS Journal of Photogrammetry & Remote Sensing* 58, 239–258.

Boser, H., I. M. Guyon & V. Vapnik (1992). A training algorithm for optimal margin classifiers. *Proceedings of the 5th Annual ACM Workshop on Computational Learning Theory*, 144–152. Pittsburgh, Pennsylvania, USA.

Brink, A. & H. Eva (2009). Monitoring 25 years of land cover change dynamics in Africa: a sample based remote sensing approach. *Applied Geography* 35: 4, 501–512.

Canty, M. J. (2010). *Image analysis, classification, and change detection in remote sensing: with algorithms for ENVI/IDL*. CRC Press, Taylos & Francis Group. Boca Raton, Florida.

Ceamanos, X. & S. Douté (2009). Spectral smile correction in CRISM hyperspectral images. *WHISPERS'09. First Workshop on Hyperspectral Image and Signal Processing: Evolution in Remote Sensing.* 26–28.8.2009, Grenoble, France.

CHIESA (2014). Climate Change Impacts on Ecosystem Services and Food Production in Eastern Africa. 20.3.2014. <*http://chiesa.icipe.org/*>.

Clark, B. J. F. & P. K. Pellikka (2009). Landscape analysis using multi-scale segmentation and object-oriented classification. In Röder, A. & J. Hill (eds.). *Recent Advances in Remote Sensing and Geoinformation Processing for Land Degradation Assessment*, 323–342. Taylor & Francis Group, London.

Clevers, J. G., S. M. De Jong, G. F. Epema, F. D. Van Der Meer, W. H. Bakker, A. K. Skidmore & K. H. Scholte (2002). Derivation of the red edge index using the MERIS standard band setting. *International Journal of Remote Sensing* 23: 16, 3169–3184.

Congalton, R. C. (1991). A review of assessing the accuracy of classifications of remotely sensed data. *Remote Sensing of Environment* 37, 35–46.

Cortes, C. & V. Vapnik (1995). Support-Vector Networks. *Machine Learning* 20, 273–297.

Elvidge, C. D. (1990). Visible and near infrared reflectance characteristics of dry plant materials. *International Journal of Remote Sensing* 11: 10, 1775–1795.

ENVI Help (2014). Exelis – Visual Information Solutions. <*http://www.exelisvis.com/docs/backgroundsvm.html*>

ENVI Support (2014). Exelis – Visual Information Solutions. <*http://www.exelisvis.com/Support/HelpArticlesDetail/TabId/219/ArtMID/900/ArticleID/4267/4267.aspx*>.

ESRI (2011). ArcGIS Desktop: Release 10. *Environmental Systems Research Institute*. Redland, CA.

Foley, J., R. DeFries, G. Asner, C. Barford, G. Bonan, S. Carpenter, F. Chapin, M. Coe, G. Daily, H. Gibbs, J. Helkowski, T. Holloway, E. Howard, C. Kucharik, C. Monfreda, J. Patz, C. Prentice, N. Ramankutty & P. Snyder (2005). Global consequences of land use. *Science* 309, 570–574.

FORMIN (2014). Ministry for Foreign Affairs of Finland. 20.3.2014. <*www.formin.fi*>.

Galvão, L. S., J. C. Epiphanio, F. M. Breunig & A. R. Formaggio (2012). Crop type discrimination using hyperspectral data. In Thenkabail, P. S., J. G. Lyon & A. Huete (eds.). *Hyperspectral remote sensing of vegetation*, 397–419. Taylor & Francis Group, Boca Raton, Florida.

Gates, D. Keegan, H. Schleted, J. & V. Weidner (1965). Spectral properties of plants. *Applied Optics* 4: 1, 11–20.

Ghosh, A., F. E. Fassnacht, P. K. Joshi & B. Koch (2014). A framework for mapping tree species combining hyperspectral and LiDAR data: role of selected classifiers and sensor across three spatial scales. *International Journal of Applied Earth Observation and Geoinformation* 26, 49–63.

Green, A. A., M. Berman, P. Switzer & M. D. Craig (1988). A transformation for ordering multispectral data in terms of image quality with implications for noise removal. *IEEE Transactions on Geoscience and Remote Sensing* 26: 1, 65–74.

Homolova, L., K. Alanko-Huotari & M. Schaepman (2009). Sensitivity of the ground-based downwelling irradiance recorded by the FODIS sensor in respect of different angular positions. *Hyperspectral Image and Signal Processing: Evolution in Remote Sensing, 2009*. 26.8–28.8 2009, WHISPERS 09 workshop. Grenoble, France.

Hughes, G. F. (1968). On the mean accuracy of statistical pattern recognizers. *IEEE Transactions on Information Theory* 14: 1, 55–63.

ICIPE (2014). International Centre of Insect Physiology and Ecology. 20.3.2014. <*www.icipe.org*>.

Jaetzold, R. & H. Schmidt (1983). Farm management handbook of Kenya. *Natural conditions and farm management information* 2 C. Ministry of Agriculture, Kenya & German Agricultural Team, German Agency for Technical Cooperation. Rossdorf, Germany.

Jensen, J. R. (2000). *Remote sensing of the environment: an earth resource perspective*. 544 pp. Prentice Hall, Upper Saddle River, New Jersey.

Kataja, K. (2012). HY Eagle 110022 FWHM calibration report. 13.9.2012. *Spectral Imaging Ltd.*. Oulu, Finland.

Kiang, N., J. Siefert, Govindjee & R. Blankenship (2007). Spectral signatures of photosynthesis. I. Review of earth organisms. *Astrobiology* 7:1, 222–251.

Kuemmerle, T., O. Chaskovskyy, J. Knorn, V. C. Radeloff, I. Kruhlov, W. S. Keeton & P. Hostert (2009). Forest cover change and illegal logging in the Ukrainian Carpathians in the transition period from 1988 to 2007. *Remote Sensing of Environment* 113, 1194–1207.

Li, X., S. Zhao, Y. Rui, & W. Tang (2007). An object-based classification approach for high-spatial resolution imagery. *Proceedings of SPIE* 6752: 3O, 1–9.

Liu, D. & F. Xia (2010). Assessing object-based classification: advantages and limitations. *Remote Sensing Letters* 1: 4, 187–194.

Melgani, F. & L. Bruzzone (2004). Classification of hyperspectral remote sensing images with support vector machines. *IEEE Transactions on Geoscience and Remote Sensing* 42: 8, 1778–1790.

MosaicMill (2014). MosaicMill Oy, Finland. 11.4.2014. <*www.mosaicmill.com*>.

Nagendra, H. & D. Rocchini (2008). High resolution satellite imagery for tropical biodiversity studies: the devil is in the detail. *Biodiversity and conservation* 17: 14, 3431–3442.

Oxford Technical Solutions (2007). *RT3000 inertial and GPS measurement system – User manual*. Oxford Technical Solutions. Oxfordshire, England.

Pal, M. & P. Watanachaturaporn (2004). Support vector machines. In Varshney, P. K. & M. J. Arora (eds.). *Advanced Image Processing Techniques for Remotely Sensed Hyperspectral Data*, 133–156. Springer. Berlin, Germany.

Pellikka, P. (2005). Taita Hills – kuivan savannin ympäröimät vehreät vuoret Kaakkois-Keniassa. *Turun yliopiston maantieteen julkaisuja* 168, 75–90.

Pellikka, P., B. Clark, T. Sirviö & K. Masalin (2005). Environmental change monitoring applying satellite and airborne remote sensing data in the Taita Hills, Kenya. *Proc. of the Int. Conf. on Remote Sensing and Geoinformation Processing in the*

Assessment and Monitoring of Land Degradation and Desertification. 7–9 September, 2005, Trier, Germany. CD-Rom publication.

Pellikka, P., M. Lötjönen, M. Siljander & L. Lens (2009). Airborne remote sensing of spatiotemporal change (1955–2004) in indigenous and exotic forest cover in the Taita Hills, Kenya. *International Journal of Applied Earth Observation and Geoinformation* 11: 221–232.

Pellikka, P., B. Clark, A. Gonsamo Gosa, N. Himberg, P. Hurskainen, E. Maeda, J. Mwang´ombe, L. Omoro & M. Siljander (2013). Agricultural expansion and its consequences in the Taita Hills, Kenya. *Developments in Earth Surface Processes* 33, 165–179.

Peltoniemi, J. I., S. Kaasalainen, J. Näränen, M. Rautiainen, P. Stenberg, H. Smolander, S. Smolander & P. Voipio (2005). BRDF measurement of understory vegetation in pine forests: dwarf shrubs, lichen and moss. *Remote Sensing of Environment* 94, 343–354.

Peñuelas, J., I. Filella, C. Biel, L. Serrano & R. Savé (1993). The reflectance at the 950–970 nm region as an indicator of plant water status. *International Journal of Remote Sensing* 14: 10, 1887–1905.

Petropoulos, G. P., C. Petropoulos & K. P. Vadrevu (2012). Support vector machines and object-based classification for obtaining land-use/cover cartography from Hyperion hyperspectral imagery. *Computers & Geosciences* 41, 99–107.

Pravilov, A. M. (2011). *Radiometry in modern scientific experiments*. p. 179. Springer, Germany.

Pu. R. (2008). An exploratory analysis of in situ hyperspectral data for broadleaf species recognition. *The International Archives of the Photogrammetry, Remote Sensing and Spatial Information Sciences* 37: B7, 255–260.

Raghuveer, M. K. & A. K. Manoj (2004). Overview of image processing. In Varshney, P. K. & M. K. Arora (eds.). *Advanced Image Processing Techniques for Remotely Sensed Hyperspectral Data*, 51–82. Heidelberg, Germany.

Rautiainen, M., M. Lang, M. Mõttus, A. Kuusk, T. Nilson, J. Kuusk & T. Lükk (2008). Multi-angular reflectance properties of a hemiboreal forest: an analysis using CHRIS PROBA data. *Remote Sensing of Environment* 112, 2627–2642.

Richter, R & D. Schläpfer (2011). *ATCOR-4 User Guide, Version 6.0.2*. ReSe Applications Schläpfer. Switzerland.

Roli, F. & G. Fumera (2001). Support vector machines for remote sensing image classification. *Proc. SPIE 4170, Image and Signal Processing for Remote Sensing*, 6: 160. 19.1 2001. Barcelona, Spain.

RSI (2004). *ENVI user's guide*. Research Systems, Inc. Boulder, Colorado.

Schaepma-Strub, G., M. E. Schaepman, T. H. Painter, S. Dangel & J. V. Martonchik (2006). Reflectance quantities in optical remote sensing – definitions and case studies. *Remote Sensing of Environment* 103, 27–42.

Schlamm, A., D. Messinger & W. Basener (2009). Geometric estimation of the inherent dimensionality of single and multi-material clusters in hyperspectral imagery. *Journal of Applied Remote Sensing* 3, 1–16.

Soini, E. (2005). Livelihood capital, strategies and outcomes in the Taita Hills of Kenya. *ICRAF Working Paper 8*. World Agroforestry Centre. Nairobi, Kenya.

Soini, E. (2006). *Livelihood, land use and environment interactions in the highlands of East Africa*. Academic dissertation. Publications of University of Helsinki Department of Geography. Helsinki, Finland.

Schaepman, M. E., R. O. Green, S. G. Ungar, B. Curtiss, J. Boardman, A. J. Plaza, B.C. Gao, S. Ustin, R. Kokaly, J. R. Miller, S. Jacquemoud, E. Ben-Dor, R. Clark, C. Davis, J. Dozier, D. G. Goodenough, D. Roverts, G. Swayze, E. J. Milton & A. F. H. Goetz (2006). The future of imaging spectroscopy – prospective technologies and applications. *Geoscience and Remote Sensing Symposium* (IGARSS 2006). 31.7– 4.8 2006, Conference paper.

Schaepman, M. E. (2009). Imaging spectrometers. In. Warner, T. A., M. D. Nellis & G. M. Foody (eds.). *The SAGE Handbook of Remote Sensing*, 166–178. SAGE Publications Ltd.

Schläpfer, D. (2011). *Parametric geocoding – Orthorectification for airborne scanner data – User Manual, Version 3.1*. ReSe Applications. Switzerland.

Specim (2009). SPECIM CaliGeo 4.9.7 AISA data processing tool – Operating manual. Spectral imaging Ltd. Oulu, Finland.

Specim (2012). AisaEAGLE datasheet ver2-2012. *Spectral Imaging Ltd*. Oulu, Finland.

Taita Research Station (2014). University of Helsinki, Taita Research Station. 6.2.2014. <*http://blogs.helsinki.fi/taita-research-station/*>.

United Nations (2012). World population prospects: the 2012 revision. *United Nations, Division of the Department of Economic and Social Affairs of the United Nations Secretariat*. <http://esa.un.org/wpp/>.

Ustin, S. L., A. A. Gitelson, S. Jacquemoud, M. Schaepman, G. P. Asner, J. A. Gamon & P. Zarco-Tejada (2009). Retrieval of foliar information about plant pigment systems from high resolution spectroscopy. *Remote Sensing of Environment* 113: 67–77.

Ustin, S. (2013). Remote sensing of canopy chemistry. *Proceedings of the National Academy of Sciences* 110: 3, 804–805.

Vapnik, V. N. (1998). *Statistical learning theory*. John Wiley & Sons. New York, USA.

Verbeiren, S. H. Eerens, I. Piccard, I. Bauwens & J. Van Orshoven (2008). Sub-pixel classification of SPOT-VEGETATION time series for the assessment of regional crop areas in Belgium. *International Journal of Applied Earth Observation and Geoinformation* 10, 486–497.

Weih, R. & N. Riggan (2010). Object-based classification vs. pixel-based classification: comparative importance of multi-resolution imagery. *The International Archives of the Photogrammetry, Remote Sensing and Spatial Information Sciences* 38: 4/C7.

Xiao. Q., S. L. Ustin & E. G. McPherson (2004). Using AVIRIS data and multiple-masking techniques to map urban forest tree species. *International Journal of Remote Sensing* 25: 24, 5637–5654.

Yarbrough, L. D., G. Easson & J. S. Kuszmaul (2005). Using at-sensor radiance and reflectance tasseled cap transforms applied to change detection for the ASTER

sensor. *Third International Workshop on the Analysis of Multi-temporal Remote Sensing Images*. Biloxi, Mississippi, USA. 16.5–18.5 2005.

Yu, Q., P. Gong, N. Clinton, G. Biging, M. Kelly & D. Schirokauer (2006). Object-based detailed vegetation classification with airborne high spatial resolution remote sensing imagery. *Photogrammetric Engineering & Remote Sensing* 72: 7, 799–811.

Zhang, C. & Z. Xie (2012). Combining object-based texture measures with a neural network for vegetation mapping in the Everglades from hyperspectral imagery. *Remote Sensing of Environment* 124, 310–320.

APPENDICES

Appendix 1. Vegetation maps of plots 16, 22, 23 and 25.

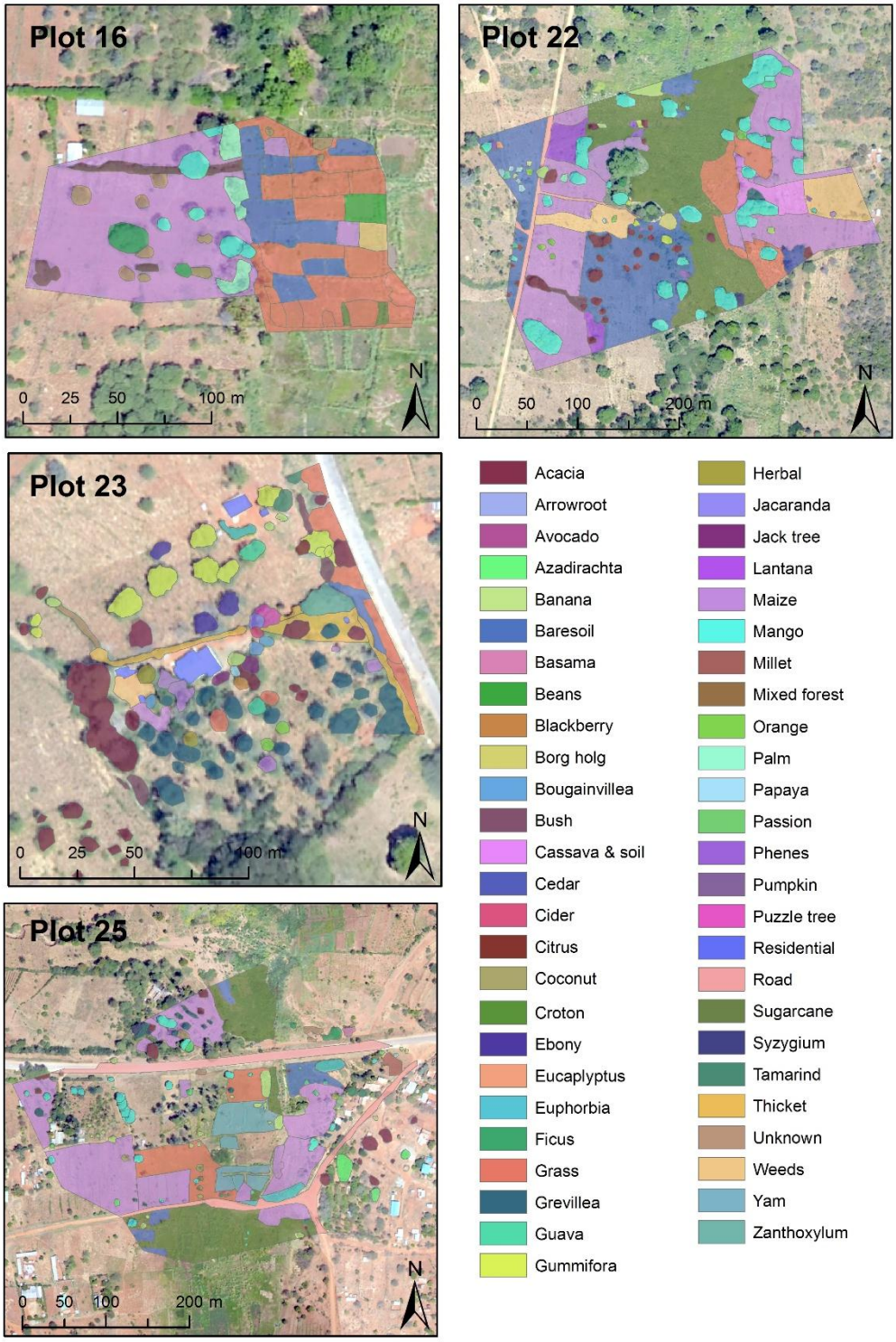

Appendix 2. Preprocessed AisaEAGLE data in true color with vegetation samples used as training and testing sets of the classification.

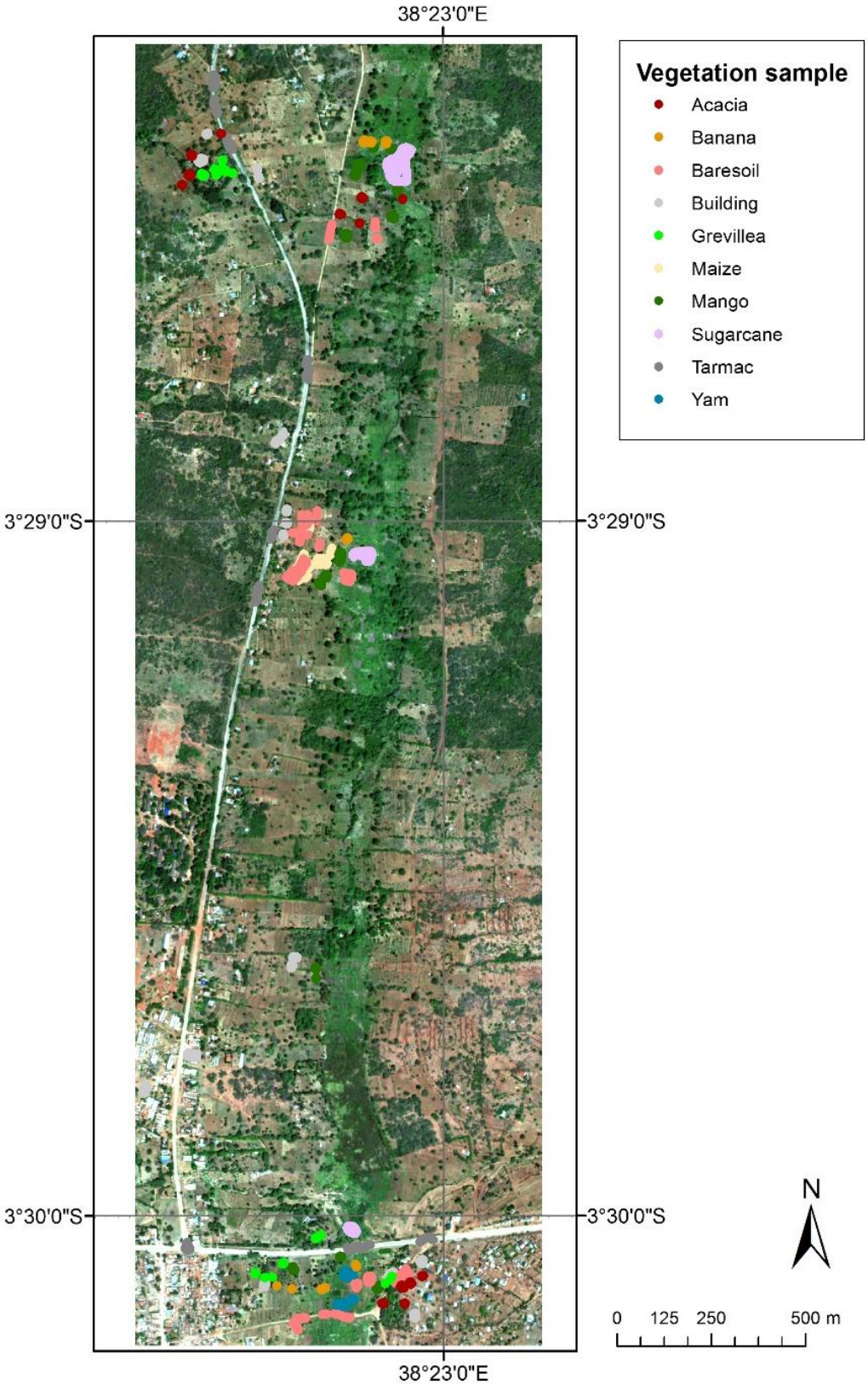

Appendix 3. Moran's I index and Eigenvalues of the MNF transformed data.

Band	Moran's I	Eigenvalue	Band	Moran's I	Eigenvalue
1	0.98	62.61	33	0.26	1.48
2	0.97	36.32	34	0.26	1.47
3	0.96	28.29	35	0.26	1.47
4	0.95	25.72	36	0.25	1.47
5	0.95	24.24	37	0.25	1.47
6	0.93	15.21	38	0.25	1.47
7	0.90	11.39	39	0.25	1.47
8	0.87	9.22	40	0.25	1.47
9	0.86	8.03	41	0.25	1.46
10	0.80	5.72	42	0.25	1.46
11	0.79	5.31	43	0.25	1.46
12	0.69	3.64	44	0.18	1.30
13	0.65	3.25	45	0.18	1.30
14	0.62	2.98	46	0.17	1.29
15	0.59	2.76	47	0.17	1.28
16	0.54	2.40	48	0.17	1.28
17	0.50	2.19	49	0.16	1.27
18	0.45	2.02	50	0.16	1.26
19	0.41	1.87	51	0.16	1.26
20	0.37	1.74	52	0.16	1.26
21	0.35	1.69	53	0.16	1.26
22	0.32	1.62	54	0.16	1.26
23	0.31	1.59	55	0.16	1.26
24	0.31	1.58	56	0.16	1.26
25	0.30	1.57	57	0.15	1.24
26	0.29	1.54	58	0.15	1.24
27	0.28	1.52	59	0.15	1.24
28	0.28	1.51	60	0.15	1.23
29	0.27	1.50	61	0.14	1.23
30	0.27	1.50	62	0.14	1.23
31	0.26	1.49	63	0.14	1.23
32	0.26	1.49	64	0.14	1.22

Appendix 4. Confusion matrix of the classification results for plot 15 with probability threshold calue 0. Columns indicate the used testing samples and rows the class where they were classified. All the pixels are classified to one of the classes.

	Maize	Sugarcane	Mango	Artificial	Bareground	Total
Unclassified	0	0	0	0	0	0
Maize	156	0	0	0	10	166
Sugarcane	0	190	0	0	0	190
Mango	0	0	125	0	0	125
Artificial	0	0	0	192	0	192
Bareground	3	0	0	0	109	112
Total	159	190	125	192	119	785

Appendix 5. Confusion matrix of the classification results for plot 15 with probability threshold value 0.90. Columns indicate the used testing samples and rows the class where they were classified. Most of the testing samples are left unclassified.

	Maize	Sugarcane	Mango	Artificial	Bareground	Total
Unclassified	151	85	85	68	111	500
Maize	8	0	0	0	0	8
Sugarcane	0	105	0	0	0	105
Mango	0	0	40	0	0	40
Artificial	0	0	0	124	0	124
Bareground	0	0	0	0	8	8
Total	159	190	125	192	119	785

Appendix 6. MNF transformed spectra for known targets based on training samples (Table 4) (grey = mean, green = std, red = min/max).